Controlled nitric oxide production via $O(^1D)$+N_2O reactions for use in oxidation flow reactor studies

Andrew Lambe[1,2], Paola Massoli[1], Xuan Zhang[1,*], Manjula Canagaratna[1], John Nowak[1,**],
Conner Daube[1], Chao Yan[3], Wei Nie[4,3], Timothy Onasch[1,2], John Jayne[1], Charles Kolb[1],
Paul Davidovits[2], Douglas Worsnop[1,3], and William Brune[5]

[1]Aerodyne Research, Inc., Billerica, Massachusetts, United States
[2]Chemistry Department, Boston College, Chestnut Hill, Massachusetts, United States
[3]Physics Department, University of Helsinki, Helsinki, Finland
[4]Joint International Research Laboratory of Atmospheric and Earth System Sciences, School of Atmospheric Sciences, Nanjing University, Nanjing, China
[5]Department of Meteorology and Atmospheric Sciences, The Pennsylvania State University, University Park, Pennsylvania, United States
[*]Current address: Atmospheric Chemistry Observations & Modeling Laboratory, National Center for Atmospheric Research, Boulder, Colorado, United States
[**]Current address: Chemistry and Dynamics Branch, NASA Langley Research Center, Hampton, Virginia, United States

Correspondence to: Andrew Lambe (lambe@aerodyne.com), William Brune (whb2@psu.edu)

Abstract.

Oxidation flow reactors that use low-pressure mercury lamps to produce hydroxyl (OH) radicals are an emerging technique for studying the oxidative aging of organic aerosols. Here, ozone (O_3) is photolyzed at 254 nm to produce $O(^1D)$ radicals, which react with water vapor to produce OH. However, the need to use parts-per-million levels of O_3 hinders the ability of oxidation flow reactors to simulate NO_x-dependent SOA formation pathways. Simple addition of nitric oxide (NO) results in fast conversion of NO_x (NO + NO_2) to nitric acid (HNO_3), making it impossible to sustain NO_x at levels that are sufficient to compete with hydroperoxy (HO_2) radicals as a sink for organic peroxy (RO_2) radicals. We developed a new method that is well suited to the characterization of NO_x-dependent SOA formation pathways in oxidation flow reactors. NO and NO_2 are produced via the reaction $O(^1D) + N_2O \rightarrow 2NO$, followed by the reaction $NO + O_3 \rightarrow NO_2 + O_2$. Laboratory measurements coupled with photochemical model simulations suggest that $O(^1D)$ + N_2O reactions can be used to systematically vary the relative branching ratio of RO_2 + NO reactions relative to RO_2 + HO_2 and/or RO_2 + RO_2 reactions over a range of conditions relevant to atmospheric SOA formation. We demonstrate proof of concept using high-resolution time-of-flight chemical ionization mass spectrometer (HR-ToF-CIMS) measurements with nitrate (NO_3^-) reagent ion to detect gas-phase oxidation products of isoprene and α-pinene previously observed in NO_x-influenced environments and in laboratory chamber experiments.

1 Introduction

Recent atmospheric observations supported by experimental and theoretical studies show that highly oxidized molecules (HOM), together with sulfuric acid, are involved in the initial nucleation steps leading to new particle formation (NPF)

(Donahue et al., 2013; Riccobono et al., 2014; Kurten et al., 2016). HOM form rapidly in the gas phase via auto-oxidation processes (Crounse et al., 2013; Rissanen et al., 2014) and tend to condense irreversibly (Ehn et al., 2014). Following NPF, semivolatile organic compounds (SVOC) with higher vapor pressures condense on newly formed aerosols at rates influenced by their volatility (Donahue et al., 2012), ultimately driving nanoparticle growth towards formation of cloud condensation nuclei (CCN) (Pierce et al., 2012; Riipinen et al., 2012). NPF events may produce as much as 50% of global CCN (Merikanto et al., 2009; Yu and Luo, 2009). However, mechanisms that govern the formation of specific HOM and condensation of SVOCs in various source regions are largely unknown.

The extent to which NPF and growth is influenced by natural and anthropogenic emissions, separately and together, is still unknown. In some locations, biogenic SOA formation is enhanced by anthropogenic carbonaceous aerosol particles, SO_x and/or NO_x (Carlton et al., 2010; Shilling et al., 2013; Xu et al., 2015). At the moment, one can only speculate about some of the possible synergistic or antagonistic chemical mechanisms regulating these processes. For example, anthropogenic emissions can enhance biogenic SOA formation by providing seed particles for condensable biogenic vapors. On the other hand, isoprene can slow down the formation of SOA from other volatile organics, possibly by depleting the local concentration of OH without itself producing significant SOA yields (Pugh et al., 2011). Globally the source strength of anthropogenic SOA is poorly constrained, with an uncertainty of at least a factor of 2 or 3 (Spracklen et al., 2011). Large uncertainties in pre-industrial aerosol emissions and processes further confound our understanding of the direct and indirect effects of anthropogenic aerosol emissions (Carslaw et al., 2014) and the impact of aerosols on climate (Andreae and Gelencsér, 2006).

To date, environmental chamber experiments have generated most of the laboratory SOA yield data used in atmospheric models, especially in simulations of polluted atmospheric conditions with elevated NO_x concentrations. However, NO_x-dependent chambers studies are complicated by the need to use multiple OH radical precursors such as hydrogen peroxide (H_2O_2) and nitrous acid (HONO) or methyl nitrite (CH_3ONO) to span the relevant range of NO_x levels (typically, H_2O_2 for low-NO_x conditions and HONO or CH_3ONO for high-NO_x conditions) (Ng et al., 2007). Additionally, chambers have relatively low throughput and are limited to residence times of several hours due to chamber deflation and/or loss of particles and oxidized vapors to the chamber walls (Zhang et al., 2014). This restricts environmental chambers to simulating atmospheric aerosol particle lifetimes and SOA yields only up to 1 or 2 days, therefore limiting the study of formation of highly oxygenated SOA characteristic of aged atmospheric organic aerosol PM (Ng et al., 2010) unless very low VOC precursor concentrations are used (Shilling et al., 2009; Pfaffenberger et al., 2013).

Oxidation flow reactors have recently been developed to study SOA formation and evolution over time scales ranging from hours to multiple days of equivalent atmospheric OH exposure. In these reactors, O_3 is photolyzed at 254 nm to produce $O(^1D)$ radicals, which react with water vapor to produce OH radicals. OH concentrations are typically $10^8\ cm^{-3}$ or greater. Under these conditions, atmospheric photochemical aging timescales up to $\sim$10 days can be simulated at flow tube residence times of a few minutes or less. Recent experimental studies suggest that flow reactor-generated SOA particles have compositions similar to SOA generated in smog chambers (Bruns et al., 2015; Lambe et al., 2015) and in the atmosphere (Tkacik et al., 2014; Ortega et al., 2016; Palm et al., 2016). Modeling studies suggest that flow reactors can simulate tropospheric oxidation reactions with minimal experimental artifacts (Li et al., 2015; Peng et al., 2015, 2016). A limitation of flow reactors is the need to use parts-per-million levels of O_3, hindering the possibility to efficiently simulate NO_x-dependent SOA formation pathways. Simple addition of NO to flow reactors, while possible (Liu et al., 2015), cannot sustain NO_x mixing ratios at levels that are sufficient to compete with hydroperoxy (HO_2) radicals as a sink for organic peroxy (RO_2) radicals due to fast conversion of NO_x to nitric acid (HNO_3) via the reactions NO + $O_3 \rightarrow NO_2$ and NO_2 + OH $\rightarrow HNO_3$. Here, we present a new method well suited to the characterization of NO_x-dependent SOA formation pathways in oxidation flow reactors. By utilizing $O(^1D)$ radicals that are generated from O_3 photolysis, we add N_2O to generate NO via the reaction $O(^1D)$ + $N_2O \rightarrow$ 2NO with no additional method modifications. We validate the concept using high-resolution time-of-flight chemical ionization mass spectrometer measurements (HR-ToF-CIMS) to detect gas-phase oxidation products of isoprene and α-pinene that have been observed in NO_x-influenced environments and laboratory chamber experiments.

2 Experimental

Experiments were conducted using an Aerodyne Potential Aerosol Mass (PAM) oxidation flow reactor, which is a horizontal 13.3 L aluminum cylindrical chamber (46 cm long × 22 cm ID) operated in continuous flow mode (Kang et al., 2007; Lambe et al., 2011a). The average residence time was 80 s. The relative humidity (RH) in the reactor was controlled in the range of 3–35 % at 22°C, corresponding to H_2O mixing ratios of approximately 0.07 - 1%. The irradiance in the reactor was measured using a photodiode (TOCON-C6, sglux Gmbh). The gas-phase SOA precursors used in these studies include two biogenic compounds (isoprene, α-pinene) that were prepared in compressed gas cylinders and introduced to the reactor at controlled rates using a mass-flow controller. Mixing ratios of the gas-phase precursors entering the reactor were 36 ppb for isoprene (diluted from 1000 ppm in N_2, Matheson) and 15 ppb for α-pinene (diluted from 150 ppm in N_2, Matheson). These mixing ratios are a factor of 3 to 10 lower than mixing ratios that are typically required to induce homogenous nucleation of condensable oxidation products in related oxidation flow reactor studies (Lambe et al., 2011b). Minimizing precursor mixing ratios also decreases the rate of RO_2 self-reactions relative to RO_2 + HO_2 and RO_2 + NO reactions. This is a goal for most laboratory experiments that is not specific to the method proposed here. However, this goal takes on added importance when RO_2 can be formed via OH, O_3 and/or NO_3 oxidation using this method as discussed in Section 2.1.

2.1 OH radical and NO_x generation

OH radicals were produced in the reactor via the reaction $O(^1D)$ + $H_2O \rightarrow$ 2OH, with $O(^1D)$ radicals produced from the reaction O_3 + h$\nu \rightarrow O_3$ + $O(^1D)$. O_3 ($\sim$1-5 ppm) was generated outside the flow reactor by O_2 irradiation at 185 nm using a mercury fluorescent lamp (GPH212T5VH, Light Sources, Inc.). $O(^1D)$ was produced by photolysis of O_3 at 254 nm inside the reactor using two or four mercury fluorescent lamps (GPH436T5L, Light Sources, Inc). A fluorescent dimming ballast was used to regulate current applied to the lamps. To vary [OH] inside the reactor, I_{254} was varied by changing the dimming voltage applied to the ballast between 1.6 and 10 VDC. At these conditions, I_{254} ranged from approximately (0.064 – 3.2) $\times 10^{15}$ ph cm^{-2} sec. The highest I_{254} value was calculated from the internal surface area of the reactor and the lamp output at maximum intensity (e.g. 10 VDC) specified by the manufacturer. Lower I_{254} values were calculated from the measured irradiance at lower dimming voltage relative to the measured irradiance and manufacturer-specified lamp output at 10 VDC.

NO and NO_2 were produced via the reaction N_2O + $O(^1D) \rightarrow$ 2NO, followed by the reaction NO + $O_3 \rightarrow NO_2$. N_2O (99.5%) was introduced from a compressed gas cylinder at flow rates ranging from 0 to 648 $\mathrm{cm^3\ min^{-1}}$, corresponding to mixing ratios of 0% to 5.6% at the carrier gas flow rates that were used. Using N_2O as the NO_x precursor has the following advantages over the simple addition of NO to the carrier gas. First, due to continuous production of $O(^1D)$ from O_3 photolysis inside the reactor (along with minor consumption of N_2O), the spatial distribution of NO and NO_2 is more homogenous. Second, attainable steady-state mixing ratios of NO from N_2O + $O(^1D)$ reactions (ppb levels) are orders of magnitude higher than simple NO injection (sub-ppt levels) as inferred from photochemical model simulations described below in Sect. 2.3.Third, photolysis of N_2O at 185 nm (if used) provides an additional source of $O(^1D)$ from the reaction N_2O + h$\nu \rightarrow N_2$ + $O(^1D)$. We assume background [NO] $<$ 0.05 ppb in the reactor based on separate [NO] measurements and calculate additional NO formed from N_2O + $O(^1D)$ reactions using the model described in Sect. 2.3. Gradients in [$O(^1D)$] due to its reaction with H_2O and N_2O may alter spatial distributions of O_x, HO_x and NO_x in the reactor. To first order, gradients in [$O(^1D)$] decrease both [HO_2] and [NO] to a similar extent, keeping the relative rates of RO_2 + HO_2 and RO_2 + NO termination pathways the same.

In most cases, oxidation of VOCs by O_3 is slower than oxidation by OH radical, even with parts per million levels of O_3 present (Peng et al., 2016). NO_3 radicals, which are produced as a byproduct of NO_2 + O_3 or HNO_3 + OH reactions, can potentially convolute interpretation of results if the relative oxidation rates of isoprene/α-pinene by OH and NO_3 are comparable. For results presented in Sects. 3.3 and 3.4, calculated OH, O_3 and NO_3 exposures combined with published OH, O_3 and NO_3 rate constants (Atkinson, 1986, 1991; Grosjean and Grosjean, 1996) suggest that the relative contribution of NO_3 to isoprene and α-pinene oxidation ranges from approximately 0 to 4% and 0 to 60%, respectively, as a function of [N_2O]. Thus, reaction rates of α-pinene with OH, O_3 and NO_3 may be comparable under a subset of experimental conditions. Potential implications are discussed in more detail in Sections 3.3.4 and 3.4.4.

2.2 NO_x and chemical ionization mass spectrometer (CIMS) measurements

In one set of experiments, [NO] and [NO_2] were measured downstream of the reactor with a Thermo Scientific Model 42i chemiluminescent analyzer and an Aerodyne Cavity Attenuated Phase Shift (CAPS) NO_2 analyzer, which measures NO_2 absorption at λ = 450 nm (Kebabian et al., 2008). During these experiments, the following operating conditions were used: $I_{254} = 4\times10^{15}$ ph $\mathrm{cm^{-2}\ sec^{-1}}$, [$O_3$] = 1 ppm, [$H_2O$] = 0.07% and 1%, [$N_2O$] = 0 to 3%. These conditions assess a subset of the attainable operating conditions for comparison with outputs of the photochemical model described in Section 2.3. The measured NO_2 mixing ratio was decreased by 10 ppb due to absorption by 1 ppm O_3 at 450 nm in the absence of NO_2. The measured NO mixing ratio was scaled by a factor of 3.2 for depletion downstream of the reactor due to 1.2 sec reaction time with 1 ppm O_3 in the sample line, assuming $k_{O_3}^{NO} = 1.8\times10^{-14}$ $\mathrm{cm^3\ molec^{-1}\ sec^{-1}}$ and pseudo-first order conditions (Atkinson et al., 2004). Additional NO depletion inside the chemiluminscent analyzer ($\sim$ 47% at 1 ppm O_3) was accounted for in a separate experiment where known mixing ratios of NO (50 ppb) and O_3 (0 to 6.9 ppm) were added at the inlet of the instrument (Fig. S1). Because the combined NO depletion in the sample line and the chemiluminscent analyzer is significantly higher at higher [O_3] (e.g. ∼90% at [O_3] = 2 ppm and ∼99.6% at [O_3] = 5 ppm), accurate experimental characterization of [NO] is more difficult above [O_3] $\sim$ 1 ppm.

In another set of experiments, mass spectra of isoprene and α-pinene gas-phase oxidation products were obtained with an Aerodyne high-resolution time-of-flight mass spectrometer (Bertram et al., 2011) coupled to an atmospheric pressure interface with a nitrate ion chemical ionization source ($\mathrm{NO_3^-}$-HRToF-CIMS, hereafter abbreviated as "$\mathrm{NO_3^-}$-CIMS") (Eisele and Tanner, 1993; Ehn et al., 2012). Nitrate ($\mathrm{NO_3^-}$) and its higher order clusters (e.g. $\mathrm{HNO_3NO_3}$) generated from x-ray ionization of $\mathrm{HNO_3}$ were used as the reagent due to the selectivity to highly oxidized organic compounds, including species that contribute to SOA formation (Ehn et al., 2014; Krechmer et al., 2015). Isoprene and α-pinene oxidation products were detected as adducts with $\mathrm{NO_3^-}$ or $\mathrm{HNO_3NO_3^-}$. CIMS data were analyzed using the Tofware software package (Tofwerk AG, Aerodyne Research, Inc.) implemented in IGOR Pro 6 (Wavemetrics, Inc.). The output of the PAM oxidation flow reactor was sampled at 10.5 $\mathrm{Lmin^{-1}}$ through a 2' length of 0.75" OD stainless steel tubing inserted directly into the rear feedthrough plate of the reactor.

Ambient $\mathrm{NO_3^-}$-CIMS measurements were conducted during the Southern Oxidant and Aerosol Study (SOAS) at the forest site in Centreville, AL (June 1 - July 15, 2013). At this site, emissions were dominated by local biogenic volatile organic compounds (BVOC) with occasional influence from nearby anthropogenic sources (Hansen et al., 2003). The mixing of biogenic and anthropogenic emissions at the foreest site promotes the formation of organic nitrates via oxidation of BVOC in the presence of $\mathrm{NO_x}$ (Lee et al., 2016).

2.3 Photochemical modeling

We used a photochemical model (Li et al., 2015; Peng et al., 2015) implemented in MATLAB (Mathworks) to calculate concentrations of radical/oxidant species produced in the reactor. Model input parameters included pressure, temperature, [H_2O], [O_3], [N_2O], I_{254}, mean residence time, and the input mixing ratios of isoprene and α-pinene. Differential equations used to describe the radical/oxidant chemistry were integrated at 5 millisecond time steps. The following reactions and associated kinetic rate constants (Sander et al., 2000, 2006) were implemented to describe $\mathrm{NO_x}$ chemistry in the reactor:

$$\mathrm{N_2O + h\nu \rightarrow N_2 + O(^1D)} \tag{R1}$$

$$\mathrm{N_2O + O(^1D) \rightarrow 2NO} \tag{R2}$$

$$\mathrm{N_2O + O(^1D) \rightarrow N_2 + O_2} \tag{R3}$$

$$\mathrm{NO + OH + M \rightarrow HONO + M} \tag{R4}$$

$$\mathrm{NO + HO_2 \rightarrow OH + NO_2} \tag{R5}$$

$$\mathrm{NO + O_3 \rightarrow NO_2 + O_2} \tag{R6}$$

$$\mathrm{NO_2 + O \rightarrow NO + O_2} \tag{R7}$$

$$\mathrm{NO_2 + O_3 \rightarrow NO_3 + O_2} \tag{R8}$$

$$\mathrm{NO_3 + O \rightarrow NO_2 + O_2} \tag{R9}$$

$$\mathrm{HONO + OH \rightarrow H_2O + NO_2} \tag{R10}$$

$$\mathrm{NO_2 + NO_3 + M \rightleftharpoons N_2O_5 + M} \tag{R11}$$

$$\mathrm{NO + NO_3 \rightarrow 2NO_2 + O_2} \tag{R12}$$

$$\mathrm{NO_2 + OH + M \rightarrow HNO_3 + M} \tag{R13}$$

$$\mathrm{NO_2 + HO_2 + M \rightarrow HNO_4 + M} \tag{R14}$$

$$\mathrm{N_2O_5 + H_2O \rightarrow 2HNO_3} \tag{R15}$$

$$\mathrm{HNO_3 + OH \rightarrow H_2O + NO_3} \tag{R16}$$

$$\mathrm{NO_3 + NO_3 \rightarrow 2NO_2 + O_2} \tag{R17}$$

The model also includes simplified $\mathrm{RO_2}$ chemistry, which is incorporated using the reactions listed below (IUPAC, 2013). The addition of these reactions constrain the effects of added isoprene or α-pinene (species "X" below) on steady-state [OH], [$\mathrm{HO_2}$] and [NO]. Second-generation organic radical products of initial organic radical reactions ("RPHO", "$\mathrm{RPO_2}$", "RPO") are not reacted further in the model.

$$\mathrm{OH + X \rightarrow RO_2 + H_2O} \tag{R18}$$

$$\mathrm{RO_2 + NO \rightarrow RO + NO_2} \tag{R19}$$

$$\mathrm{RO_2 + HO_2 \rightarrow ROOH + O_2} \tag{R20}$$

$$\mathrm{ROOH + OH \rightarrow RO_2 + H_2O} \tag{R21}$$

$$\mathrm{ROOH + OH \rightarrow RPHO + OH + H_2O} \tag{R22}$$

$$\mathrm{RO_2 + OH \rightarrow RPO_2 + H_2O} \tag{R23}$$

$$\mathrm{RO_2 + RO_2 \rightarrow ROOR} \tag{R24}$$

$$\mathrm{RO + O_2 \rightarrow RPO + HO_2} \tag{R25}$$

$$\mathrm{RO_2 + NO + M \rightarrow RO_2NO + M} \tag{R26}$$

$$\mathrm{RO + NO + M \rightarrow RONO + M} \tag{R27}$$

$$\mathrm{RO + NO_2 + M \rightarrow RONO_2 + M} \tag{R28}$$

Calculated OH exposures (product of mean OH concentration and residence time) ranged from 1.7×10^{10} to 2.1×10^{12} molec $\mathrm{cm^{-3}}$ sec or approximately 3 hours to 16 days of equivalent atmospheric exposure at [OH] = 1.5×10^{6} $\mathrm{cm^{-3}}$ (Mao et al., 2009). Steady-state [NO] and [HO_2] ranged from 0 to 13.5 ppb and 0.01 to 2.1 ppb, respectively, depending on [N_2O], [H_2O], [O_3] and I_{254}. We assumed ±25% uncertainty in the calculated OH exposure and ±60% uncertainty in other model outputs (Peng et al., 2015). For ratios of model outputs with independent ±60% uncertainties (e.g. NO:HO_2), propagated uncertainties of ±85% were assumed. Addition of N_2O at the highest mixing ratios that were used suppressed [OH] because N_2O competes with H_2O as a sink for $O(^1D)$. Potential consequences of OH suppression are discussed where applicable in Sects. 3.3 and 3.4.

3 Results and Discussion

3.1 Comparison of measured and modeled [NO] and [NO_2] values following $O(^1D)$ + N_2O and NO + O_3 reactions

Figure 1 compares modeled and measured NO mixing ratios obtained following 80 sec residence time in the reactor at the operating conditions described in Sect.2.2. The corresponding integrated OH exposures are approximately 2.6×10^{11} and 2.4×10^{12} molec $\mathrm{cm^{-3}}$ sec, respectively, in the absence of added N_2O. Symbols are colored by [N_2O] which ranged from 0 to 3%. Measured [NO] ranged from 0 to 10.4 ppb and increased with increasing [N_2O], as expected, at both [H_2O] = 0.07% and 1%. The mean ratio of modeled-measured [NO] was 0.94 ± 0.19 at [H_2O] = 0.07% and 3.85 ± 2.33 at [H_2O] = 1%.

NO_2, which is formed by the NO + O_3 reaction, is more straightforward to measure under these conditions because NO_2 reacts approximately 500 times slower than NO with O_3. Thus, a comparison of modeled and measured [NO_2] provides additional method evaluation with less uncertainty than [NO] measurements. Figure 2 compares corresponding modeled and measured NO_2 mixing ratios obtained during the same experiments described in Figure 1. As expected, [NO_2] increased with increasing [N_2O] because of faster NO + O_3 reaction rate from increasing [NO]. At [H_2O] = 0.07%, measured [NO_2] ranged from 0 to 291 ppb, whereas at [H_2O] = 1%, measured [NO_2] ranged from 0 to 59 ppb. [NO_2] was lower in the latter case because additional OH was formed from $O(^1D)$ + H_2O reactions (Section 2.1), which increased the rate of the OH + NO_2 reaction. The mean ratio of modeled-measured [NO_2] was 0.72 ± 0.39 at [H_2O] = 0.07% and 1.05 ± 0.50 at [H_2O] = 1%. These results, combined with results shown in Figure 1, suggest that an uncharacterized H_2O- or HNO_3-related artifact negatively biased the measured [NO] values at [H_2O] = 1%, and that the photochemical model described in Section 2.3 may be used to evaluate a wider range of reactor operating conditions. The model also constrains mixing ratios of radical species such as HO_2 that are difficult to measure directly or require additional measurement techniques (Mauldin et al., 1999; Sanchez et al., 2016).

3.2 Optimal reactor operating conditions for $O(^1D)$ + N_2O + reactions

To investigate optimal operating conditions for NO_x generation, we implemented the model described in Sect. 2.3 over operating conditions I_{254} = 3.2×10^{13} to 6.4×10^{15} ph cm^{-2} sec^{-1}, [O_3] = 0.5 to 50 ppm, and [H_2O] = 0.07 to 2.3% at 22°C, respectively, as a function of [N_2O] = 0 to 5%. These values span the nominal range of operating conditions that can be achieved with the PAM reactor. To facilitate independent evaluation of the effects of [O_3] and I_{254} on [NO], we restricted our analysis to conditions that use only 254 nm photolysis. Using both 185 and 254 nm photolysis provides additional sources of $O(^1D)$ and OH from N_2O and H_2O photolysis at 185 nm, respectively, at the expense of independent control of [O_3] and I_{254}.

Figure 3 shows the modeled steady-state [NO] in the reactor as a function of [N_2O] = 0 to 5%, assuming a mean residence time of 80 sec, [H_2O] = 1%, and [O_3] = 5 ppm. In addition, Figs. S1 - S3 in the Supplement show modeled NO:HO_2 and OH:NO_3 ratios as a function of input [N_2O], with I_{254}, [O_3], and [H_2O] each varied individually while other input conditions are fixed. The following observations that are obtained from Figs. 3 and S1 - S3 were used to identify the optimal operating conditions:

1. At fixed [O_3], [H_2O], and [N_2O], [$O(^1D$] and [NO] increase with increasing I_{254} (Figs. 3 and S1).
2. At fixed I_{254}, [H_2O], and [N_2O], increasing O_3 increases the production and loss rates of NO from N_2O + $O(^1D)$ and NO + O_3 reactions, respectively. The relative importance of NO + OH, NO + O_3, and NO + NO_3 reactions, which depend on [N_2O] and [O_3], further influence [NO]:
   - At [N_2O] $\sim$ 1%, increasing [O_3] from 0.5 to 5 ppm increases [NO] because the reaction rate of NO + OH decreases relative to NO + O_3 (Fig. S2a).
   - At [N_2O] $>$ 1%, increasing [O_3] from 5 to 50 ppm decreases [NO] because the reaction rate of NO + NO_3 increases relative to NO + O_3 (Fig. S2a).
3. At fixed I_{254}, [H_2O], and [N_2O], increasing [O_3] decreases [NO]:[HO_2] and [OH]:[NO_3] by increasing NO_2 and NO_3 formation from NO + O_3 and NO_2 + O_3reactions.

4. At fixed I_{254}, $[O_3]$, and $[N_2O]$, increasing $[H_2O]$ increases $[OH]$:$[NO_3]$ by increasing OH production from H_2O + $O(^1D)$ reactions (Fig. S3).

The relative importance of these operating conditions is situationally dependent on the relative OH, O_3, and NO_3 rate constants of the target species and photochemical age. To demonstrate proof of principle, we present NO_3^--CIMS spectra of isoprene and α-pinene oxidation products in the following sections.

3.3 NO_3^--CIMS spectra of isoprene oxidation products

Figure 4 shows NO_3^--CIMS mass spectra of products generated from the oxidation of isoprene (C_5H_8) that cluster with NO_3^- ions to form NO_3^--species adducts. Ion signals are plotted as a function of mass-to-charge ratio (m/Q). NO_3 adduct formation is a relatively low-energy process that does not result in fragmentation of the analyte (Eisele and Tanner, 1993; Kurtén et al., 2011). Thus, the measured ion signals are directly related to the chemical formulas of individual species that are generated in the reactor. Ion signals corresponding to isoprene oxidation products shown in Fig. 4 were colored based on classification in ion groups containing 2-5 carbon atoms with zero ($C_4H_{4,6,8}O_{4-7}$ and $C_5H_{6,8,10,12}O_{3-8}$), one ($C_{2-3}H_{3,5}NO_5$ and $C_5H_{7,9,11}NO_{6-11}$), and two ($C_5H_{10}N_2O_{8-10}$) nitrogen atoms, where we assumed that nitrogen atoms were associated with nitrate functional groups and not heterocyclic compounds. We also assume that nitrate functional groups are formed from RO_2 + NO or RO_2 + NO_2 reactions (Sect. 2.1). To examine changes in relative contributions of $C_4H_{4,6,8}O_{4-7}$, $C_5H_{6,8,10,12}O_{3-8}$, $C_5H_{7,9,11}NO_{6-11}$, and $C_5H_{10}N_2O_{8-10}$ ions as a function of added NO_x, we made two simplifying assumptions: (1) the NO_3^--CIMS had the same sensitivity to all species that were detected, and (2) HNO_3 generated in the reactor did not alter the relative selectivity of the CIMS to different classes of oxidation products, as has been observed in some cases (Hyttinen et al., 2015).

To generate spectra shown in Fig. 4, the reactor was operated at I_{254} = 6.4×10^{13} and 3.2×10^{15} ph cm^{-2} sec^{-1}, $[H_2O]$ = 1%, and $[N_2O]$ = 0 and 3%. As shown in Figs. S4 and S5, corresponding OH exposures ranged from $(1.7 – 2.0)\times10^{10}$ (Fig. 4a and 4c; calculated $>$ 82% of isoprene reacted) and $(0.52 – 2.1)\times10^{12}$ molec cm^{-3} sec (Fig. 4b and 4d; calculated $\sim$ 100% of isoprene reacted), respectively. At low OH exposure, the OH suppression at “high NO_x” relative to “low NO_x” was comparatively minor (15%), whereas at high OH exposure, the OH suppression at “high NO_x” relative to ‘low NO_x” was larger (75%). At the “high-NO_x” OH exposure of 5.2×10^{11} molec cm^{-3} sec, isoprene can react with OH up to 52 times in the reactor. This presumably exceeds the number of OH reactions (followed by RO_2 + NO reactions) that are necessary to fragment or condense oxidation products to the point where they are no longer detected with NO_3^--CIMS. Thus, it is unlikely that OH suppression at “high OH” and “high NO_x” significantly affected the NO_3^--CIMS spectra shown in Fig. 4. To aid interpretation of results shown in Fig. 4, Fig. 5 summarizes several known isoprene + OH reaction pathways that are terminated by reactions of RO_2 with HO_2, NO, or NO_2. As will be discussed in the following sections, these pathways yield multigenerational oxidation products with chemical formulas corresponding to the major ions that are plotted in Fig. 4.

3.3.1 NO_3^--CIMS spectral features observed at “low NO_x” conditions

$C_{4-5}H_{4-12}O_{3-8}$ ions comprised 93% and 97% of the signals at low and high OH exposure (Figs. 4a and Fig. 4c, respectively). The $C_5H_{7-11}NO_{6-11}$ signals that were observed here may be due to background NO_x in the reactor (Sect. 2.1). The signal at m/Q = 230, $C_5H_{12}O_6$ (NO_3^- omitted for brevity here and elsewhere), was the largest signal detected at both low and high OH exposures at “low-NO_x” conditions. Figure 5 suggests this species is a second-generation oxidation product generated from two reactions with OH and two RO_2 + HO_2 termination reactions (Krechmer et al., 2015; St. Clair et al., 2016) and is typically associated with isoprene SOA formation and growth under “low-NO_x” conditions. (Liu et al., 2016) Signals in Figs. 4b and 4d are approximately 10 times higher than in Figs. 4a and 4c because additional OH exposure produces higher yields of multi-generation oxidation products that are detected with NO_3^--CIMS.

Previously-identified multi-generation isoprene oxidation products such as $C_5H_{10}O_5$, $C_5H_{12}O_5$, and $C_5H_{10}O_6$ (Surratt et al., 2006; Krechmer et al., 2015; St. Clair et al., 2016) were also detected at significant intensity under low-NO_x conditions. These species are formed after two reactions with OH, one RO_2+ HO_2 termination reaction and one RO_2 + RO_2 termination reaction (Fig. 5). When the OH exposure was increased from 2.0×10^{10} to 2.1×10^{12} molec cm^{-3} sec, the signal at $C_5H_{12}O_6$ increased by a factor of 10 and the signal at m/Q = 246, $C_5H_{12}O_7$, increased by a factor of 5. At high OH exposure, $C_5H_{12}O_7$ was the second-largest peak in the spectrum. These highly oxygenated isoprene oxidation products are likely also important in SOA formation processes. $C_5H_{10}O_7$ is a proposed tri-hydroperoxy carbonyl product formed after one reaction with OH, two hydrogen shifts and one RO_2 + HO_2 termination reaction as shown in Fig. 5 (Peeters et al., 2014).

We hypothesize two reasons for the prominence of $C_5H_{10}O_7$, $C_5H_{12}O_7$, and $C_5H_{10}O_8$ in our spectra. First, NO_3^- is more selective to highly oxidized species than other reagent ions (Surratt et al., 2006; Liu et al., 2016). Second, higher OH exposures were achieved in the reactor than in environmental chambers. For example, the spectra shown in Figs. 4a and 4b were obtained at integrated OH exposures of 1.7×10^{10} and 2.1×10^{12} molec cm^{-3} sec, respectively, compared to an OH exposure of 8.6×10^9 molec cm^{-3} sec in the environmental chamber NO_3^--CIMS measurements conducted by Krechmer et al. (2015).

3.3.2 NO_3^--CIMS spectral features observed at “high NO_x” conditions

Following addition of N_2O at ~3% mixing ratio, the NO_3^--CIMS spectra changed significantly at low and high OH exposures (Figs. 4b and 4d). The signals of $C_{4-5}H_{4-12}O_{3-8}$ oxidation products decreased, although the $C_4H_{4,6,8}O_{4-7}$: $C_5H_{6,8,10,12}O_{3-8}$ ratio increased, presumably due to decomposition of alkoxy (RO) radicals generated from C_5 RO_2 + NO reactions into C_4 products. The $C_{2-3}H_{3,5}NO_5$ (peroxy acetyl nitrate and peroxy propionyl nitrate), $C_5H_{7,9,11}NO_{6-11}$ and $C_5H_{10}N_2O_{8-10}$ signals increased. At low OH exposure, $C_{2-3}H_{3,5}NO_5$, $C_5H_{7,9,11}NO_{6-11}$ and $C_5H_{10}N_2O_{8-10}$ signals constituted 2%, 38% and 7% of the NO_3^--CIMS signals, respectively (Fig. 4c). The largest signal in this spectrum was m/Q = 259, $C_5H_{11}NO_7$. Fig. 5 suggests this compound is a second-generation oxidation product that is formed after two reactions with OH, one RO_2 + NO termination reaction and one RO_2 + HO_2 termination reaction (Xiong et al., 2015). The signal observed at m/Q = 288, $C_5H_{10}N_2O_8$, is a second-generation oxidation product that is formed after two reactions with OH and two RO_2 + NO termination reactions (Fig. 5) (Xiong et al., 2015). Other ion signals associated with dinitrate species included m/Q =

304, $C_5H_{10}N_2O_9$, and m/Q = 320, $C_5H_{10}N_2O_{10}$. Related signals were detected at m/Q = 351 and 367 (not shown), which we assume represent $(HNO_3NO_3^-)C_5H_{10}N_2O_8$ and $(HNO_3NO_3^-)C_5H_{10}N_2O_9$ because we are not aware of other feasible $(NO_3^-)C_5$ adducts at these mass-to-charge ratios.

At high OH exposure, the same $C_5H_{7,9,11}NO_{6-11}$ and $C_5H_{10}N_2O_{8-10}$ species observed at low OH exposure were detected, but at higher concentrations and at higher dinitrate:nitrate. This is presumably due to higher NO:HO_2 achieved at higher I_{254} and fixed [N_2O] (Figs. 3, S2, S5-S6). $C_{2-3}H_{3,5}NO_5$, $C_5H_{7,9,11}NO_{6-11}$ and $C_5H_{10}N_2O_{8-10}$ signals made up 0.3%, 33% and 56%, respectively, of the NO_3^--CIMS spectrum shown in Fig. 4d, where $C_5H_{10}N_2O_8$ was the largest signal that is detected.

To demonstrate our ability to mimic atmospheric NO_x-dependent photochemistry, Figures 4e and 4f show $C_4H_{4,6,8}O_{4-7}$, $C_5H_{6,8,10,12}O_{3-8}$, $C_{2-3}H_{3,5}NO_5$, $C_5H_{7,9,11}NO_{6-11}$, and $C_5H_{10}N_2O_{8-10}$ ion signals detected in NO_3^--CIMS spectra at the SOAS ground site in Centreville, Alabama, USA. The spectra shown were obtained on 25 Jun 2013 (0730-1100) and 4-5 Jul 2013 (1200 – 0000) which represented periods with sustained "high" and "low" NO mixing ratios of 0.53 ± 0.17 ppb and 0.024 ± 0.025 ppb, respectively, measured at the site. Figures 4a, 4c and 4e indicate that adding N_2O to the reactor increases the similarity between the composition of isoprene oxidation products generated at lower photochemical age in the reactor (Figs. 4a and 4c) and under "low-NO" ambient conditions (Fig. 4e). Likewise, Figures 4b, 4d and 4f indicate that adding N_2O to the reactor increases the similarity between the composition of isoprene oxidation products generated at higher photochemical age in the reactor (Figs. 4b and 4d) and at "high-NO" ambient conditions (Fig. 4f). $(HNO_3NO_3^-)C_5H_{10}N_2O_{8-9}$ adducts were also observed in Fig. 4f (not shown).

3.3.3 Influence of acylperoxy nitrates from RO_2 + NO_2 reactions

Acylperoxy nitrates (APNs) may be generated from reactions of aldehydic, biogenic VOC oxidation products with OH followed by RO_2 + NO_2 termination reactions, e.g. LaFranchi et al. (2009). Peroxy acetyl nitrate (PAN, $C_2H_3NO_5$) and propionyl peroxy nitrate (PPN, $C_3H_5NO_5$), are minor components (<2%) of the spectra shown in Figs. 4c - 4f. A comparison of Figs. 4c and 4e suggests that yields of PAN and PPN are not enhanced in the reactor compared to atmospheric conditions. Additional APNs may be generated following the OH oxidation of methacrolein, a first-generation isoprene oxidation product. Methacryloyl peroxy nitrate (MPAN, $C_4H_5NO_5$) is a second-generation oxidation product formed after one methacrolein + OH reaction and one RO_2 + NO_2 termination reaction (Orlando et al., 1999). C4-hydroxynitrate-PAN ($C_4H_6N_2O_9$) is a third-generation oxidation product formed through the methacrolein channel after three reactions with OH, two RO_2 + NO termination reactions and one RO_2 + NO_2 termination reaction (Surratt et al., 2010). Neither $C_4H_5NO_5$ nor $C_4H_6N_2O_9$ were detected in the laboratory and ambient NO_3^--CIMS spectra shown in Figs. 4c - 4f. Either these compounds were oxidized or thermally decomposed prior to detection, or their signals were below detection limit. $C_4H_7NO_5$, which is formed after one methacrolein + OH reaction and one RO_2 + NO termination reaction (Surratt et al., 2010), was detected (Fig. 5). Taken together, these observations suggest that yields of APNs were not significantly enhanced in the reactor compared to atmospheric conditions.

3.3.4 Influence of isoprene + NO_3 reactions

Based on the calculated isoprene + OH and isoprene + NO_3 reaction rates (Figs. S5-S6) we assume that isoprene + NO_3 reactions were a minor influence on the NO_3^--CIMS spectra shown in Figs. 4c and 4d. This assumption is further supported by the similarity between laboratory and ambient NO_3^--CIMS spectra, the latter of which was obtained during the daytime and thus with minimal NO_3 exposure (0730 - 1100 for "high-NO" spectra shown in Fig. 4f). Specific operating conditions different than those used in this study could increase the relative influence of isoprene + NO_3 reactions. In this hypothetical situation, enhanced yields of $C_5H_7NO_5$, $C_5H_8N_2O_8$ and $C_5H_{10}N_2O_8$ might occur following two reactions with NO_3 (Rollins et al., 2009). In addition, $C_5H_{10}N_2O_9$ may be generated from one isoprene + NO_3 reaction followed by one RO_2 + HO_2 termination reaction (Schwantes et al., 2015). All four of these ions are detected in the spectra shown in Fig. 4, although $C_5H_8N_2O_8$ (not shown in Fig. 4) is present at 0.5% of the intensity of $C_5H_{10}N_2O_8$. If $C_5H_8N_2O_8 : C_5H_{10}N_2O_8$ is significantly different under NO_3-dominated conditions, this ratio could distinguish the relative rates of isoprene + OH and isoprene + NO_3 reactions. Otherwise, it is not clear that the expected product distributions are significantly different whether isoprene is oxidized by OH or NO_3 in the presence of NO_x.

3.4 NO_3^--CIMS spectra of α-pinene oxidation products

Figure 6 shows NO_3^--CIMS mass spectra of products generated from the oxidation of α-pinene ($C_{10}H_{16}$). Ion signals corresponding to α-pinene oxidation products were colored based on classification in $C_5H_{6,8}O_{5-7}$, $C_{6-9}H_{8,10,12,14}O_{6-12}$, $C_{10}H_{14,16,18}O_{5-14}$, and $C_{19-20}H_{28,30,32}O_{9-18}$ ion groups containing zero nitrogen atoms; $C_{2-3}H_{3,5}NO_5$, $C_5H_7NO_{6-11}$, $C_{6-9}H_{9,11,13,15}NO_{5-10}$, and $C_{10}H_{15,17}NO_{4-14}$ ion groups containing one nitrogen atom; and a $C_{10}H_{16,18}N_2O_{6-13}$ ion group containing two nitrogen atoms. As was the case with isoprene oxidation products, we assumed nitrogen atoms present in α-pinene oxidation products were associated with nitrate functional groups formed from RO_2 + NO or RO_2 + NO_2 reactions. Additionally, we again assumed the NO_3^--CIMS had the same sensitivity to all species that were detected, and that HNO_3 generated in the reactor did not alter the relative selectivity of the CIMS to different classes of oxidation products. Because the oxidation pathways leading to α-pinene-derived HOM are signficantly more complex than those leading to isoprene-derived HOM, the analogous figure to Fig. 5 for α-pinene-derived HOM is beyond the scope of this paper.

To generate spectra shown in Fig. 6, the reactor was operated at $I_{254} = 2.8\times10^{15}$ ph $cm^{-2}sec^{-1}$, $[H_2O]$ = 0.07%, and $[N_2O]$ = 0 and 3.2%. In this experiment, lower $[H_2O]$ was used to minimize [OH] and facilitate closer comparison with spectra from previous NO_3^--CIMS studies of α-pinene + O_3 oxidation products generated at "low-NO_x" conditions (Ehn et al., 2012, 2014). As shown in Fig. S7, corresponding OH and O_3 exposures ranged from $(0.19 – 1.8)\times10^{11}$ molec cm^{-3} sec and $(7.2\text{-}9.5)\times10^{16}$ molec cm^{-3} sec for the low- and high-NO_x conditions, respectively. To first order, at OH and O_3 exposures of 2.1×10^{10} and 7.4×10^{15} molec cm^{-3} sec that are attained at $[N_2O]$ = 3.2%, α-pinene should react once with each oxidant in the gas phase. Thus, at the highest $[N_2O]$ used, yields of second-generation (or later) α-pinene + OH oxidation products detected with the NO_3^--CIMS were minimized relative to α-pinene + O_3 first-generation oxidation products, as desired (Jokinen et al., 2015). However, a potential consequence of using $O(^1D)$ + N_2O reactions to study the NO_x-dependence of chemical systems similar to those examined by Ehn et al. (2012, 2014) is that RO_2 may be produced from α-pinene + NO_3 reactions in addition to α-pinene + O_3 or α-pinene + OH reactions (Sect. 2.1 and Fig. S7).

3.4.1 NO_3^--CIMS mass spectral features observed at "low NO_x" conditions

$C_5H_{6,8}O_{5-7}$, $C_{6-9}H_{8,10,12,14}O_{6-12}$, $C_{10}H_{14,16,18}O_{5-14}$, and $C_{19-20}H_{28,30,32}O_{9-18}$ ion groups comprised 5%, 36%, 46%, and 4% of the signal detected at "low-NO_x" conditions (Fig. 6a), assuming equal CIMS sensitivity and transmission to all detected species . The C_{10} monomers and C_{19-20} dimers compounds that were observed are often associated with atmospheric new particle formation events (Ehn et al., 2014). The prominent $C_{10}H_{14,16}O_{7-9}$ signals detected at m/Q = 308, 310, 324, 326, 340 and 342 in our measurements were dominant signals in previous laboratory and field experiments influenced by the ozonolysis of α-pinene emissions (Ehn et al., 2010, 2012, 2014; Jokinen et al., 2015). Other signals that were observed correspond to C_{5-9} species that were generated following carbon-carbon bond cleavage of the C_{10} backbone (Ehn et al., 2012). The remaining ~10% of the signal was classified into $C_{2-3}H_{3,5}NO_5$, $C_5H_7NO_{6-11}$, $C_{6-9}H_{9,11,13,15}NO_{5-10}$, and $C_{10}H_{15,17}NO_{4-14}$ ion groups and may be due to background NO_x in the reactor (Sect. 2.1).

3.4.2 NO_3^--CIMS mass spectral features observed at "high NO_x" conditions

As was the case with NO_3^--CIMS spectra of isoprene oxidation products, the addition of N_2O to the reactor significantly changed the mass spectrum of α-pinene oxidation products (Fig. 6b). At [N_2O] = 3.2%, organic nitrates and dinitrates comprised 65% of the total ion signal. We observed reduction in $C_{6-9}H_{8,10,12,14}O_{6-12}$, $C_{10}H_{14,16,18}O_{5-14}$, and $C_{19-20}H_{28,30,32}O_{9-18}$ signals, along with increases in $C_5H_{6,8}O_{5-7}$, $C_5H_7O_{6-11}$, $C_{6-9}H_{9,11,13,15}NO_{5-10}$, $C_{10}H_{15,17}NO_{4-14}$ and $C_{10}H_{16,18}N_2O_{6-13}$ signals. The C_{10} dinitrates may originate from two α-pinene + OH reactions followed by two RO_2 + NO reactions, but may also include contributions from one α-pinene + NO_3 reaction followed by one RO_2 + NO reaction. The largest signal in Fig. 6b was observed at m/Q = 240, $C_5H_6O_7$. The largest organic nitrate signals in this spectrum were at m/Q = 329, $C_8H_{13}NO_9$, followed by $C_{10}H_{15}NO_9$ (m/Q = 355), $C_{10}H_{16}N_2O_9$ (m/Q = 354), and $C_{10}H_{15}NO_8$ (m/Q = 339).

Figure 6c shows $C_5H_6O_{5-7}$, $C_{6-9}H_{8,10,12,14}O_{6-12}$, $C_{10}H_{14,16,18}O_{5-14}$, $C_{19-20}H_{28,30,32}O_{9-18}$, $C_{2-3}H_{3,5}NO_5$, $C_5H_7NO_{6-11}$, $C_{6-9}H_{9,11,13,15}NO_{5-10}$, $C_{10}H_{15,17}NO_{4-14}$, and $C_{10}H_{16,18}N_2O_{6-13}$ signals detected with NO_3^--CIMS at the Centreville site during the SOAS campaign. The spectra shown here were obtained during the sampling period shown in Fig. 4f and, given the large number of compounds, may include contributions from HOM precursors other than α-pinene. A comparison of Figs. 6a-6c indicates that adding N_2O to the reactor increases the similarity between the composition of α-pinene oxidation products generated in the reactor and under "high-NO" ambient conditions, especially in regards to the enhanced $C_5H_6O_{5-7}$, $C_{6-9}H_{9,11,13,15}NO_{5-10}$, $C_{10}H_{15,17}NO_{4-14}$, and $C_{10}H_{16,18}N_2O_{6-13}$ signals.

3.4.3 Detection of acylperoxy nitrates from RO_2 + NO_2 reactions

Figs. 6b and 6c indicate that PAN (m/Q = 183, $C_2H_3NO_5$) and PPN (m/Q = 197, $C_3H_5NO_5$) are formed at lower yields (<0.4%) than were observed with isoprene (Fig. 4c and 4d), suggesting that PAN and PPN formation from reaction of α-pinene-derived–RO_2 with NO_2 are not enhanced in the reactor compared to atmospheric conditions. $C_9H_{13}NO_6$ and $C_{10}H_{15}NO_{6-8}$ are APNs generated following OH oxidation of pinonaldehyde, a major first-generation oxidation product of α-pinene, with termination by RO_2 + NO_2 reaction (Eddingsaas et al., 2012). All four compounds are detected in the reactor and ambient NO_3^--CIMS spectra shown in Figs. 6b and 6c, with $C_{10}H_{15}NO_{6-8}$ signals among the largest in the spectra. If these signals represent APNs, they appear to be important in both laboratory and atmospheric conditions.

3.4.4 Influence of α-pinene + NO_3 reactions

Our calculations suggest that α-pinene + NO_3 reactions compete with α-pinene + OH reactions at the experimental conditions used to generate the NO_3^-–CIMS spectrum shown in Fig. 6b (Fig. S7). If this were the case, enhanced yields of $C_{10}H_{15}NO_6$ are anticipated from α-pinene + NO_3 reaction to generate pinonaldehyde, followed by pinonaldehyde + NO_3 reaction and RO_2 + NO_2 termination (Perraud et al., 2010; Nah et al., 2016) Other minor α-pinene + NO_3 products detected with CIMS include $C_{10}H_{15}NO_5$, $C_9H_{13}NO_6$, $C_{10}H_{16}N_2O_7$, and $C_{10}H_{15}NO_9$ (Nah et al., 2016). We hypothesize that if α-pinene + NO_3 reactions influence the spectrum shown in Fig. 6b, $C_{10}H_{15}NO_6 : C_{10}H_{15}NO_8$ should be higher in Fig. 6b than in Fig. 6c. Instead, the $C_{10}H_{15}NO_6 : C_{10}H_{15}NO_8$ ratio was 0.12 in the reactor and 0.28 at the Centreville site during a daytime period (0730 - 1100) with presumably negligible NO_3 influence.

Dinitrates ($C_{10}H_{16,18}N_2O_{6-13}$) shown in Fig. 6b may originate from two α-pinene + OH reactions followed by two RO_2 + NO terminations, or one α-pinene + NO_3 reaction followed by one RO_2 + NO termination. Given comparable calculated OH and NO_3 reaction rates under these conditions (Fig. S7e), we hypothesize that the majority of dinitrate signals should originate from α-pinene + NO_3 reactions if their yields are not oxidant-dependent. If this were the case, $C_{10}H_{16,18}N_2O_{6-13}$: $C_{10}H_{15,17}NO_{4-14}$ should be larger in Fig. 6b than in Fig. 6c. However, $C_{10}H_{16,18}N_2O_{6-13}$: $C_{10}H_{15,17}NO_{4-14}$ was 0.23 in the reactor and 0.61 at the Centreville site. Thus, while the calculated α-pinene + NO_3 oxidation rate is significant (Fig. S7e), it is not clear that α-pinene + NO_3 oxidation products significantly affect the spectrum shown in Fig. 6b. This may be due to significantly lower organic nitrate yields from α-pinene + NO_3 than from α-pinene + OH reactions in the presence of NO (Fry et al., 2014; Rindelaub et al., 2015).

3.5 Transition from RO_2+HO_2 to RO_2+NO-dominant regimes observed in isoprene and α-pinene oxidation products

Figures 7 and 8 shows normalized signals of the representative groups of isoprene and α-pinene oxidation products as a function of increasing NO:HO_2, which may be influenced by NO + HO_2, NO + RO_2 and HO_2 + RO_2 reactions in the reactor. For each group of compounds, signals obtained at a specific NO:HO_2 were normalized to the maximum observed signal. NO:HO_2 is correlated with the relative branching ratios of RO_2 + HO_2 and RO_2 + NO reactions that govern the distribution of oxidation products observed in Figs. 4 and 6. As is evident from Figs. 7 and 8, different ion families were characterized by different trends as a function of NO:HO_2. The normalized signals of C_{4-5} (isoprene), C_{6-10} (α-pinene) and C_{19-20} (α-pinene) species decreased monotonically with increasing NO:HO_2. In Fig. 8, the abundance of C_{19-20} dimers decreased significantly faster than the C_{6-10} species. Because dimers are products of RO_2 + RO_2 self-reactions, their yield is quadratic with respect to $[RO_2]$ and therefore was more affected by competing RO_2 + NO reactions than species formed from RO_2 + HO_2 reactions.

The normalized signals of C_5 (isoprene) and C_{10} (α-pinene) organic nitrates reached their maximum values at NO:$HO_2 \approx$ 1 prior to decreasing. Maximum signals of C_{6-9} organic nitrates (α-pinene) were obtained at NO:HO_2 = 2.4, and maximum signals of C_5 (isoprene) and C_{10} (α-pinene) dinitrates were obtained at NO:HO_2 = 5.2 and 6.4. The formation of dinitrates was favored when RO_2 + NO >> RO_2 + HO_2, as expected, and regardless of whether RO_2 was formed from oxidation of α-pinene by OH, O_3 or NO_3. We hypothesize that NO:HO_2 >> 1 favored RO_2 + NO $\rightarrow$ RO + NO_2 fragmentation reactions that led to formation of smaller, more volatile $C_5H_{6-8}O_{5-7}$ and $C_5H_7NO_{6-11}$ α-pinene oxidation products (Atkinson, 2007; Chacon-Madrid and Donahue, 2011), whose signals continuously increased with increasing NO:HO_2, along with other products not detected with NO_3^--CIMS. This pathway apparently competed with RO_2 + NO $\rightarrow$ RO_2NO reactions that led to formation of C_5 isoprene dinitrates, C_6-C_{10} α-pinene nitrates and C_{10} α-pinene dintrates.

Isoprene oxidation products such as $C_5H_9NO_7$ and $C_5H_{11}NO_7$ contain one peroxide and one nitrate functional group, and $C_5H_9NO_8$ contains two peroxides and one nitrate functional group. The formation of these species, as well as C_{6-10} α-pinene-derived organic nitrates, was favored at NO:$HO_2 \approx$ 1-2 where the relative rates of RO_2 + NO and RO_2 + HO_2 reactions were similar. This correlation suggests that the C_{6-10} α-pinene organic nitrates detected with NO_3^--CIMS contained a combination of peroxide and nitrate functional groups, whereas C_5 (isoprene) and C_{10} (α-pinene) dinitrates contained fewer functional groups that were specifically formed from RO_2 + HO_2 reactions.

4 Atmospheric Implications

The use of $O(^1D)$ + N_2O reactions facilitates systematic control of NO:HO_2 over the range of “RO_2 + HO_2 dominant” to “RO_2 + NO dominant” conditions. Further, this is accomplished with the use of a single OH radical precursor (O_3) that has previously hindered characterization of NO_x-dependent chemistry in oxidation flow reactors. Our results suggest that this method can be used to identify molecular tracers for processes influenced by RO_2 + NO and/or RO_2 + NO_2 reactions (Figs. 4 and 6). This method will be used in future work to investigate the influence of NO_x on physicochemical properties of secondary organic aerosols such as hygroscopicity and refractive indices over an atmospherically relevant range of NO:HO_2. Care should be taken to use experimental conditions that minimize the relative contributions of unwanted NO_3-initiated oxidation chemistry – for example, $[O_3]$ >> 5 ppm and $[H_2O]$ << 1% (Figs. S2 and S3) – particularly when using species such as α-pinene that are highly reactive to NO_3. While potential formation of dinitrates from α-pinene + NO_3 reactions at high-NO conditions was not the primary goal of this experiment, we note that this chemical fingerprint has been observed in ambient measurements (Yan et al., 2016) and thus represents an additional application of $O(^1D)$ + N_2O reactions in future work. Additionally, studies that require multiple days of equivalent atmospheric OH oxidation at NO:HO_2 >>1 should consider implementing 185 nm photolysis of H_2O and N_2O to provide additional sources of $O(^1D)$ and OH that may decrease OH suppression due to competing $O(^1D)$ + H_2O and $O(^1D)$ + N_2O reactions.

Acknowledgements. This research was supported by the Atmospheric Chemistry Program of the U.S. National Science Foundation under grants AGS-1536939, AGS-1537446 and AGS-1537009 and by the U.S. Office of Science (BER), Department of Energy (Atmospheric Systems Research) under grants DE-SC0006980 and DE-SC0011935. A. T. Lambe thanks Gabriel Isaacman-VanWertz and Jesse Kroll (Massachusetts Institute of Technology) for helpful discussion, Zhe Peng and Jose Jimenez (University of Colorado - Boulder) for preliminary input on method operation with added λ = 185 nm radiation, and Karsten Baumann and Eric Edgerton (Atmospheric Research and Analysis, Inc.) for the use of ambient NO measurements during the SOAS campaign.

References

Andreae, M. O. and Gelencsér, A.: Black carbon or brown carbon? The nature of light-absorbing carbonaceous aerosols, Atmospheric Chemistry and Physics, 6, 3131–3148, 2006.

Atkinson, R.: Kinetics and mechanisms of the gas-phase reactions of the hydroxyl radical with organic compounds under atmospheric conditions, Chemical Reviews, 86, 69–201, 1986.

Atkinson, R.: Kinetics and Mechanisms of the Gas-Phase Reactions of the NO_3 Radical with Organic Compounds, Journal of Physical and Chemical Reference Data, 20, 459–507, doi:http://dx.doi.org/10.1063/1.555887, http://scitation.aip.org/content/aip/journal/jpcrd/20/3/10.1063/1.555887, 1991.

Atkinson, R.: Rate constants for the atmospheric reactions of alkoxy radicals: An updated estimation method, Atmospheric Environment, 41, 8468–8485, 2007.

Atkinson, R., Baulch, D. L., Cox, R. A., Crowley, J. N., Hampson, R. F., Hynes, R. G., Jenkin, M. E., Rossi, M. J., and Troe, J.: Evaluated kinetic and photochemical data for atmospheric chemistry: Volume I - gas phase reactions of O_x, HO_x, NO_x and SO_x species, Atmospheric Chemistry and Physics, 4, 1461–1738, doi:10.5194/acp-4-1461-2004, http://www.atmos-chem-phys.net/4/1461/2004/, 2004.

Bertram, T. H., Kimmel, J. R., Crisp, T. A., Ryder, O. S., Yatavelli, R. L. N., Thornton, J. A., Cubison, M. J., Gonin, M., and Worsnop, D. R.: A field-deployable, chemical ionization time-of-flight mass spectrometer, Atmospheric Measurement Techniques, 4, 1471–1479, 2011.

Bruns, E. A., Krapf, M., Orasche, J., Huang, Y., Zimmermann, R., Drinovec, L., Močnik, G., El Haddad, I., Slowik, J. G., Dommen, J., Baltensperger, U., and Prevot, A. S. H.: Characterization of primary and secondary wood combustion products generated under different burner loads, Atmospheric Chemistry and Physics, 15, 2825–2841, 2015.

Carlton, A., Pinder, R., Bhave, P., and Pouliot, G.: To What Extent Can Biogenic SOA be Controlled?, Environmental Science and Technology, 44, 3376–3380, 2010.

Carslaw, K. S., Lee, L. A., Reddington, C. L., Pringle, K. J., Rap, A., Forster, P. M., Mann, G. W., Spracklen, D. V., Woodhouse, M. T., Regayre, L. A., and Pierce, J. R.: Large contribution of natural aerosols to uncertainty in indirect forcing, Nature, 503, 67–71, 2014.

Chacon-Madrid, H. J. and Donahue, N. M.: Fragmentation vs. functionalization: chemical aging and organic aerosol formation, Atmospheric Chemistry and Physics, 11, 10 553–10 563, 2011.

Crounse, J. D., Nielsen, L. B., Jørgensen, S., Kjaergaard, H. G., and Wennberg, P. O.: Autoxidation of Organic Compounds in the Atmosphere, The Journal of Physical Chemistry Letters, 4, 3513–3520, 2013.

Donahue, N. M., Kroll, J. H., Pandis, S. N., and Robinson, A. L.: A two-dimensional volatility basis set – Part 2: Diagnostics of organic-aerosol evolution, Atmospheric Chemistry and Physics, 12, 615–634, 2012.

Donahue, N. M., Ortega, I. K., Chuang, W., Riipinen, I., Riccobono, F., Schobesberger, S., Dommen, J., Baltensperger, U., Kulmala, M., Worsnop, D. R., and Vehkamäki, H.: How do organic vapors contribute to new-particle formation?, Faraday Discussions, 165, 91, 2013.

Eddingsaas, N. C., Loza, C. L., Yee, L. D., Seinfeld, J. H., and Wennberg, P. O.: α-pinene photooxidation under controlled chemical conditions – Part 1: Gas-phase composition in low- and high-NO_x environments, Atmospheric Chemistry and Physics, 12, 6489–6504, 2012.

Ehn, M., Junninen, H., Petäjä, T., Kurtén, T., Kerminen, V.-M., Schobesberger, S., Manninen, H. E., Ortega, I. K., Vehkamäki, H., Kulmala, M., and Worsnop, D. R.: Composition and temporal behavior of ambient ions in the boreal forest, Atmospheric Chemistry and Physics, 10, 8513–8530, 2010.

Ehn, M., Kleist, E., Junninen, H., Petäjä, T., Lönn, G., Schobesberger, S., Dal Maso, M., Trimborn, A., Kulmala, M., Worsnop, D. R., Wahner, A., Wildt, J., and Mentel, T. F.: Gas phase formation of extremely oxidized pinene reaction products in chamber and ambient air, Atmospheric Chemistry and Physics, 12, 5113–5127, 2012.

Ehn, M., Thornton, J. A., Kleist, E., Sipilä, M., Junninen, H., Pullinen, I., Springer, M., Rubach, F., Tillmann, R., Lee, B., Lopez-Hilfiker, F., Andres, S., Acir, I.-H., Rissanen, M., Jokinen, T., Schobesberger, S., Kangasluoma, J., Kontkanen, J., Nieminen, T., Kurten, T., Nielsen, L. B., Jørgensen, S., Kjaergaard, H. G., Canagaratna, M., Maso, M. D., Berndt, T., Petäjä, T., Wahner, A., Kerminen, V.-M., Kulmala, M., Worsnop, D. R., Wildt, J., and Mentel, T. F.: A large source of low-volatility secondary organic aerosol, Nature, 506, 476–479, 2014.

Eisele, F. L. and Tanner, D. J.: Measurement of the gas phase concentration of H_2SO_4 and methane sulfonic acid and estimates of H_2SO_4 production and loss in the atmosphere, Journal of Geophysical Research: Atmospheres, 98, 9001–9010, doi:10.1029/93JD00031, http://dx.doi.org/10.1029/93JD00031, 1993.

Fry, J. L., Draper, D. C., Barsanti, K. C., Smith, J. N., Ortega, J., Winkler, P. M., Lawler, M. J., Brown, S. S., Edwards, P. M., Cohen, R. C., and Lee, L.: Secondary Organic Aerosol Formation and Organic Nitrate Yield from NO_3 Oxidation of Biogenic Hydrocarbons, Environmental Science & Technology, 48, 11 944–11 953, doi:10.1021/es502204x, http://dx.doi.org/10.1021/es502204x, pMID: 25229208, 2014.

Grosjean, E. and Grosjean, D.: Rate constants for the gas-phase reaction of ozone with 1, 1-disubstituted alkenes, International Journal of Chemical Kinetics, 28, 911–918, doi:10.1002/(SICI)1097-4601(1996)28:12<911::AID-KIN8>3.0.CO;2-Q, http://dx.doi.org/10.1002/(SICI)1097-4601(1996)28:12<911::AID-KIN8>3.0.CO;2-Q, 1996.

Hansen, D. A., Edgerton, E. S., Hartsell, B. E., Jansen, J. J., Kandasamy, N., Hidy, G. M., and Blanchard, C. L.: The Southeastern Aerosol Research and Characterization Study: Part 1–Overview, Journal of the Air & Waste Management Association, 53, 1460–1471, 2003.

Hyttinen, N., Kupiainen-Määttä, O., Rissanen, M. P., Muuronen, M., Ehn, M., and Kurtén, T.: Modeling the Charging of Highly Oxidized Cyclohexene Ozonolysis Products Using Nitrate-Based Chemical Ionization, The Journal of Physical Chemistry A, 119, 6339–6345, doi:10.1021/acs.jpca.5b01818, http://dx.doi.org/10.1021/acs.jpca.5b01818, pMID: 26023711, 2015.

IUPAC: Data sheets for reactions of gas-phase organic peroxy radicals, http://iupac.pole-ether.fr/index.html, 2013.

Jokinen, T., Berndt, T., Makkonen, R., Kerminen, V.-M., Junninen, H., Paasonen, P., Stratmann, F., Herrmann, H., Guenther, A. B., Worsnop, D. R., Kulmala, M., Ehn, M., and Sipilä, M.: Production of extremely low volatile organic compounds from biogenic emissions: Measured yields and atmospheric implications, Proceedings of the National Academy of Sciences, 112, 7123–7128, 2015.

Kang, E., Root, M. J., Toohey, D. W., and Brune, W. H.: Introducing the concept of potential aerosol mass (PAM), Atmospheric Chemistry and Physics, 7, 5727–5744, 2007.

Kebabian, P. L., Wood, E. C., Herndon, S. C., and Freedman, A.: A Practical Alternative to Chemiluminescence-Based Detection of Nitrogen Dioxide: Cavity Attenuated Phase Shift Spectroscopy, Environmental Science & Technology, 42, 6040–6045, doi:10.1021/es703204j, http://dx.doi.org/10.1021/es703204j, pMID: 18767663, 2008.

Krechmer, J. E., Coggon, M. M., Massoli, P., Nguyen, T. B., Crounse, J. D., Hu, W., Day, D. A., Tyndall, G. S., Henze, D. K., Rivera-Rios, J. C., Nowak, J. B., Kimmel, J. R., Mauldin, III, R. L., Stark, H., Jayne, J. T., Sipilä, M., Junninen, H., Clair, J. M. S., Zhang, X., Feiner, P. A., Zhang, L., Miller, D. O., Brune, W. H., Keutsch, F. N., Wennberg, P. O., Seinfeld, J. H., Worsnop, D. R., Jimenez, J. L., and Canagaratna, M. R.: Formation of Low Volatility Organic Compounds and Secondary Organic Aerosol from Isoprene Hydroxyhydroperoxide Low-NO Oxidation, Environmental Science and Technology, 49, 10 330–10 339, 2015.

Kurtén, T., Petäjä, T., Smith, J., Ortega, I. K., Sipilä, M., Junninen, H., Ehn, M., Vehkamäki, H., Mauldin, L., Worsnop, D. R., and Kulmala, M.: The effect of H_2SO_4 & amine clustering on chemical ionization mass spectrometry (CIMS) measurements of gas-phase sulfuric acid, Atmospheric Chemistry and Physics, 11, 3007–3019, doi:10.5194/acp-11-3007-2011, http://www.atmos-chem-phys.net/11/3007/2011/, 2011.

Kurten, T., Tiusanen, K., Roldin, P., Rissanen, M., Luy, J.-N., Boy, M., Ehn, M., and Donahue, N.: α-Pinene Autoxidation Products May Not Have Extremely Low Saturation Vapor Pressures Despite High O:C Ratios, The Journal of Physical Chemistry A, 120, 2569–2582, 2016.

LaFranchi, B. W., Wolfe, G. M., Thornton, J. A., Harrold, S. A., Browne, E. C., Min, K. E., Wooldridge, P. J., Gilman, J. B., Kuster, W. C., Goldan, P. D., de Gouw, J. A., McKay, M., Goldstein, A. H., Ren, X., Mao, J., and Cohen, R. C.: Closing the peroxy acetyl nitrate budget: observations of acyl peroxy nitrates (PAN, PPN, and MPAN) during BEARPEX 2007, Atmospheric Chemistry and Physics, 9, 7623–7641, doi:10.5194/acp-9-7623-2009, http://www.atmos-chem-phys.net/9/7623/2009/, 2009.

Lambe, A. T., Ahern, A. T., Williams, L. R., Slowik, J. G., Wong, J. P. S., Abbatt, J. P. D., Brune, W. H., Ng, N. L., Wright, J. P., Croasdale, D. R., Worsnop, D. R., Davidovits, P., and Onasch, T. B.: Characterization of aerosol photooxidation flow reactors: heterogeneous oxidation, secondary organic aerosol formation and cloud condensation nuclei activity measurements, Atmospheric Measurement Techniques, 4, 445–461, 2011a.

Lambe, A. T., Onasch, T. B., Massoli, P., Croasdale, D. R., Wright, J. P., Ahern, A. T., Williams, L. R., Worsnop, D. R., Brune, W. H., and Davidovits, P.: Laboratory studies of the chemical composition and cloud condensation nuclei (CCN) activity of secondary organic aerosol (SOA) and oxidized primary organic aerosol (OPOA), Atmospheric Chemistry and Physics Discussions, 11, 13 617–13 653, 2011b.

Lambe, A. T., Chhabra, P. S., Onasch, T. B., Brune, W. H., Hunter, J. F., Kroll, J. H., Cummings, M. J., Brogan, J. F., Parmar, Y., Worsnop, D. R., Kolb, C. E., and Davidovits, P.: Effect of oxidant concentration, exposure time, and seed particles on secondary organic aerosol chemical composition and yield, Atmospheric Chemistry and Physics, 15, 3063–3075, 2015.

Lee, B. H., Mohr, C., Lopez-Hilfiker, F. D., Lutz, A., Hallquist, M., Lee, L., Romer, P., Cohen, R. C., Iyer, S., Kurten, T., Hu, W., Day, D. A., Campuzano-Jost, P., Jimenez, J. L., Xu, L., Ng, N. L., Guo, H., Weber, R. J., Wild, R. J., Brown, S. S., Koss, A., De Gouw, J., Olson, K., Goldstein, A. H., Seco, R., Kim, S., McAvey, K., Shepson, P. B., Starn, T., Baumann, K., Edgerton, E. S., Liu, J., Shilling, J. E., Miller, D. O., Brune, W., Schobesberger, S., D'Ambro, E. L., and Thornton, J. A.: Highly functionalized organic nitrates in the southeast United States: Contribution to secondary organic aerosol and reactive nitrogen budgets, Proceedings of the National Academy of Sciences, 113, 1516–1521, 2016.

Li, R., Palm, B. B., Ortega, A. M., Hlywiak, J., Hu, W., Peng, Z., Day, D. A., Knote, C., Brune, W. H., De Gouw, J. A., and Jimenez, J. L.: Modeling the Radical Chemistry in an Oxidation Flow Reactor: Radical Formation and Recycling, Sensitivities, and the OH Exposure Estimation Equation, The Journal of Physical Chemistry A, 119, 150406123535 006, 2015.

Liu, J., D'Ambro, E. L., Lee, B. H., Lopez-Hilfiker, F. D., Zaveri, R. A., Rivera-Rios, J. C., Keutsch, F. N., Iyer, S., Kurten, T., Zhang, Z., Gold, A., Surratt, J. D., Shilling, J. E., and Thornton, J. A.: Efficient Isoprene Secondary Organic Aerosol Formation from a Non-IEPOX Pathway, Environmental Science & Technology, 50, 9872–9880, doi:10.1021/acs.est.6b01872, http://dx.doi.org/10.1021/acs.est.6b01872, pMID: 27548285, 2016.

Liu, P. F., Abdelmalki, N., Hung, H.-M., Wang, Y., Brune, W. H., and Martin, S. T.: Ultraviolet and visible complex refractive indices of secondary organic material produced by photooxidation of the aromatic compounds toluene and *m*-xylene, Atmospheric Chemistry and Physics, 15, 1435–1446, 2015.

Mao, J., Ren, X., Brune, W., Olson, J., Crawford, J., Fried, A., Huey, L., Cohen, R., Heikes, B., and Singh, H.: Airborne measurement of OH reactivity during INTEX-B, Atmospheric Chemistry and Physics, 9, 163–173, 2009.

Mauldin, R. L., Tanner, D. J., and Eisele, F. L.: Measurements of OH during PEM-Tropics A, Journal of Geophysical Research: Atmospheres, 104, 5817–5827, doi:10.1029/98JD02305, http://dx.doi.org/10.1029/98JD02305, 1999.

Merikanto, J., Spracklen, D. V., Mann, G. W., Pickering, S. J., and Carslaw, K. S.: Impact of nucleation on global CCN, Atmospheric Chemistry and Physics, 9, 8601–8616, 2009.

Nah, T., Sanchez, J., Boyd, C. M., and Ng, N. L.: Photochemical Aging of α-pinene and β-pinene Secondary Organic Aerosol formed from Nitrate Radical Oxidation, Environmental Science & Technology, 50, 222–231, doi:10.1021/acs.est.5b04594, http://dx.doi.org/10.1021/acs.est.5b04594, pMID: 26618657, 2016.

Ng, N. L., Chhabra, P. S., Chan, A., Surratt, J. D., Kroll, J. H., Kwan, A. J., McCabe, D. C., Wennberg, P. O., Sorooshian, A., and Murphy, S. M.: Effect of NO_x level on secondary organic aerosol (SOA) formation from the photooxidation of terpenes, Atmospheric Chemistry and Physics, 7, 5159–5174, 2007.

Ng, N. L., Canagaratna, M. R., Zhang, Q., Jimenez, J. L., Tian, J., Ulbrich, I. M., Kroll, J. H., Docherty, K. S., Chhabra, P. S., Bahreini, R., Murphy, S. M., Seinfeld, J. H., Hildebrandt, L., Donahue, N. M., Decarlo, P. F., Lanz, V. A., Prévôt, A. S. H., Dinar, E., Rudich, Y., and Worsnop, D. R.: Organic aerosol components observed in Northern Hemispheric datasets from Aerosol Mass Spectrometry, Atmospheric Chemistry and Physics, 10, 4625–4641, 2010.

Orlando, J. J., Tyndall, G. S., and Paulson, S. E.: Mechanism of the OH-initiated oxidation of methacrolein, Geophysical Research Letters, 26, 2191–2194, doi:10.1029/1999GL900453, http://dx.doi.org/10.1029/1999GL900453, 1999.

Ortega, A. M., Hayes, P. L., Peng, Z., Palm, B. B., Hu, W., Day, D. A., Li, R., Cubison, M. J., Brune, W. H., Graus, M., Warneke, C., Gilman, J. B., Kuster, W. C., De Gouw, J., Gutiérrez-Montes, C., and Jimenez, J. L.: Real-time measurements of secondary organic aerosol formation and aging from ambient air in an oxidation flow reactor in the Los Angeles area, Atmospheric Chemistry and Physics, 16, 7411–7433, 2016.

Palm, B. B., Campuzano-Jost, P., Ortega, A. M., Day, D. A., Kaser, L., Jud, W., Karl, T., Hansel, A., Hunter, J. F., Cross, E. S., Kroll, J. H., Peng, Z., Brune, W. H., and Jimenez, J. L.: In situ secondary organic aerosol formation from ambient pine forest air using an oxidation flow reactor, Atmospheric Chemistry and Physics, 16, 2943–2970, 2016.

Peeters, J., Müller, J.-F., Stavrakou, T., and Nguyen, V. S.: Hydroxyl Radical Recycling in Isoprene Oxidation Driven by Hydrogen Bonding and Hydrogen Tunneling: The Upgraded LIM1 Mechanism, The Journal of Physical Chemistry A, 118, 8625–8643, 2014.

Peng, Z., Day, D. A., Stark, H., Li, R., Lee-Taylor, J., Palm, B. B., Brune, W. H., and Jimenez, J. L.: HO_x radical chemistry in oxidation flow reactors with low-pressure mercury lamps systematically examined by modeling, Atmospheric Measurement Techniques, 8, 4863–4890, 2015.

Peng, Z., Day, D. A., Ortega, A. M., Palm, B. B., Hu, W., Stark, H., Li, R., Tsigaridis, K., Brune, W. H., and Jimenez, J. L.: Non-OH chemistry in oxidation flow reactors for the study of atmospheric chemistry systematically examined by modeling, Atmospheric Chemistry and Physics, 16, 4283–4305, 2016.

Perraud, V., Bruns, E. A., Ezell, M. J., Johnson, S. N., Greaves, J., and Finlayson-Pitts, B. J.: Identification of Organic Nitrates in the NO_3 Radical Initiated Oxidation of α-Pinene by Atmospheric Pressure Chemical Ionization Mass Spectrometry, Environmental Science & Technology, 44, 5887–5893, doi:10.1021/es1005658, http://dx.doi.org/10.1021/es1005658, pMID: 20608721, 2010.

Pfaffenberger, L., Barmet, P., Slowik, J. G., Praplan, A. P., Dommen, J., Prevot, A. S. H., and Baltensperger, U.: The link between organic aerosol mass loading and degree of oxygenation: an α-pinene photooxidation study, Atmospheric Chemistry and Physics, 13, 6493–6506, 2013.

Pierce, J. R., Leaitch, W. R., Liggio, J., Westervelt, D. M., Wainwright, C. D., Abbatt, J. P. D., Ahlm, L., Al-Basheer, W., Cziczo, D. J., Hayden, K. L., Lee, A. K. Y., Li, S.-M., Russell, L. M., Sjostedt, S. J., Strawbridge, K. B., Travis, M., Vlasenko, A., Wentzell, J. J. B., Wiebe, H. A., Wong, J. P. S., and Macdonald, A. M.: Nucleation and condensational growth to CCN sizes during a sustained pristine biogenic SOA event in a forested mountain valley, Atmospheric Chemistry and Physics, 12, 3147–3163, 2012.

Pugh, T. A. M., MacKenzie, A. R., Langford, B., Nemitz, E., Misztal, P. K., and Hewitt, C. N.: The influence of small-scale variations in isoprene concentrations on atmospheric chemistry over a tropical rainforest, Atmospheric Chemistry and Physics, 11, 4121–4134, 2011.

Riccobono, F., Schobesberger, S., Scott, C. E., Dommen, J., Ortega, I. K., Rondo, L., Almeida, J., Amorim, A., Bianchi, F., Breitenlechner, M., David, A., Downard, A., Dunne, E. M., Duplissy, J., Ehrhart, S., Flagan, R. C., Franchin, A., Hansel, A., Junninen, H., Kajos, M., Keskinen, H., Kupc, A., Kürten, A., Kvashin, A. N., Laaksonen, A., Lehtipalo, K., Makhmutov, V., Mathot, S., Nieminen, T., Onnela, A., Petäjä, T., Praplan, A. P., Santos, F. D., Schallhart, S., Seinfeld, J. H., Sipilä, M., Spracklen, D. V., Stozhkov, Y., Stratmann, F., Tomé, A., Tsagkogeorgas, G., Vaattovaara, P., Viisanen, Y., Vrtala, A., Wagner, P. E., Weingartner, E., Wex, H., Wimmer, D., Carslaw, K. S., Curtius, J., Donahue, N. M., Kirkby, J., Kulmala, M., Worsnop, D. R., and Baltensperger, U.: Oxidation Products of Biogenic Emissions Contribute to Nucleation of Atmospheric Particles, Science, 344, 717–721, 2014.

Riipinen, I., Yli-Juuti, T., Pierce, J. R., Petäjä, T., Worsnop, D. R., Kulmala, M., and Donahue, N. M.: The contribution of organics to atmospheric nanoparticle growth, Nature Publishing Group, 5, 453–458, 2012.

Rindelaub, J. D., McAvey, K. M., and Shepson, P. B.: The photochemical production of organic nitrates from α-pinene and loss via acid-dependent particle phase hydrolysis, Atmospheric Environment, 100, 193 – 201, doi:http://dx.doi.org/10.1016/j.atmosenv.2014.11.010, http://www.sciencedirect.com/science/article/pii/S1352231014008693, 2015.

Rissanen, M. P., Kurten, T., Sipilä, M., Thornton, J. A., Kangasluoma, J., Sarnela, N., Junninen, H., Jørgensen, S., Schallhart, S., Kajos, M. K., Taipale, R., Springer, M., Mentel, T. F., Ruuskanen, T., Petäjä, T., Worsnop, D. R., Kjaergaard, H. G., and Ehn, M.: The Formation of Highly Oxidized Multifunctional Products in the Ozonolysis of Cyclohexene, J. Am. Chem. Soc, 136, 15 596–15 606, 2014.

Rollins, A., Kiendler-Scharr, A., Fry, J., Brauers, T., Brown, S., Dorn, H., Dubé, W., Fuchs, H., Mensah, A., and Mentel, T.: Isoprene oxidation by nitrate radical: alkyl nitrate and secondary organic aerosol yields, Atmospheric Chemistry and Physics, 9, 6685–6703, 2009.

Sanchez, J., Tanner, D. J., Chen, D., Huey, L. G., and Ng, N. L.: A new technique for the direct detection of HO_2 radicals using bromide chemical ionization mass spectrometry (Br-CIMS): initial characterization, Atmospheric Measurement Techniques, 9, 3851–3861, doi:10.5194/amt-9-3851-2016, http://www.atmos-meas-tech.net/9/3851/2016/, 2016.

Sander, S., Friedl, R., DeMore, W., Golden, D., Kurylo, M., Hampson, R. F., Huie, R., Moortgat, G., Ravishankara, A., Kolb, C., and Molina, M. J.: Chemical Kinetics and Photochemical Data for Use in Stratospheric Modeling, Evaluation Number 13, JPL Publication, pp. 1–74, 2000.

Sander, S., Friedl, R., Golden, D., Kurylo, M., Moortgat, G., Keller-Rudek, H., Wine, P., Ravishankara, A. R., Kolb, C., Molina, M., Finlayson-Pitts, B., Huie, R., and Orkin, V.: Chemical Kinetics and Photochemical Data for Use in Atmospheric Studies, Evaluation Number 15, JPL Publication, pp. 1–523, 2006.

Schwantes, R. H., Teng, A. P., Nguyen, T. B., Coggon, M. M., Crounse, J. D., St Clair, J. M., Zhang, X., Schilling, K. A., Seinfeld, J. H., and Wennberg, P. O.: Isoprene + NO_3 Oxidation Products from the RO_2 + HO_2 Pathway, The Journal of Physical Chemistry A, 119, 10 158–10 171, 2015.

Shilling, J., Chen, Q., King, S., Rosenoern, T., Kroll, J., Worsnop, D., Decarlo, P., Aiken, A., Sueper, D., and Jimenez, J.: Loading-dependent elemental composition of alpha-pinene SOA particles, Atmospheric Chemistry and Physics, 9, 771–782, 2009.

Shilling, J. E., Zaveri, R. A., Fast, J. D., Kleinman, L., Alexander, M. L., Canagaratna, M. R., Fortner, E., Hubbe, J. M., Jayne, J. T., Sedlacek, A., Setyan, A., Springston, S., Worsnop, D. R., and Zhang, Q.: Enhanced SOA formation from mixed anthropogenic and biogenic emissions during the CARES campaign, Atmospheric Chemistry and Physics, 13, 2091–2113, 2013.

Spracklen, D. V., Jimenez, J. L., Carslaw, K. S., Worsnop, D. R., Evans, M. J., Mann, G. W., Zhang, Q., Canagaratna, M. R., Allan, J., Coe, H., McFiggans, G., Rap, A., and Forster, P.: Aerosol mass spectrometer constraint on the global secondary organic aerosol budget, Atmospheric Chemistry and Physics, 11, 12 109–12 136, 2011.

St. Clair, J. M., Rivera-Rios, J. C., Crounse, J. D., Knap, H. C., Bates, K. H., Teng, A. P., Jørgensen, S., Kjaergaard, H. G., Keutsch, F. N., and Wennberg, P. O.: Kinetics and Products of the Reaction of the First-Generation Isoprene Hydroxy Hydroperoxide (ISOPOOH) with OH, The Journal of Physical Chemistry A, 120, 1441–1451, 2016.

Surratt, J., Murphy, S., Kroll, J., Ng, N., Hildebrandt, L., Sorooshian, A., Szmigielski, R., Vermeylen, R., Maenhaut, W., and Claeys, M.: Chemical composition of secondary organic aerosol formed from the photooxidation of isoprene, The Journal of Physical Chemistry A, 110, 9665–9690, 2006.

Surratt, J. D., Chan, A. W. H., Eddingsaas, N. C., Chan, M., Loza, C. L., Kwan, A. J., Hersey, S. P., Flagan, R. C., Wennberg, P. O., and Seinfeld, J. H.: Reactive intermediates revealed in secondary organic aerosol formation from isoprene, Proceedings of the National Academy of Sciences, 107, 6640–6645, doi:10.1073/pnas.0911114107, http://www.pnas.org/content/107/15/6640.abstract, 2010.

Tkacik, D. S., Lambe, A. T., Jathar, S., Li, X., Presto, A. A., Zhao, Y., Blake, D., Meinardi, S., Jayne, J. T., Croteau, P. L., and Robinson, A. L.: Secondary Organic Aerosol Formation from in-Use Motor Vehicle Emissions Using a Potential Aerosol Mass Reactor, Environmental Science and Technology, 48, 11 235–11 242, 2014.

Xiong, F., McAvey, K. M., Pratt, K. A., Groff, C. J., Hostetler, M. A., Lipton, M. A., Starn, T. K., Seeley, J. V., Bertman, S. B., Teng, A. P., Crounse, J. D., Nguyen, T. B., Wennberg, P. O., Misztal, P. K., Goldstein, A. H., Guenther, A. B., Koss, A. R., Olson, K. F., De Gouw, J. A., Baumann, K., Edgerton, E. S., Feiner, P. A., Zhang, L., Miller, D. O., Brune, W. H., and Shepson, P. B.: Observation of isoprene hydroxynitrates in the southeastern United States and implications for the fate of NO_x, Atmospheric Chemistry and Physics, 15, 11 257–11 272, 2015.

Xu, L., Guo, H., Boyd, C. M., Klein, M., Bougiatioti, A., Cerully, K. M., Hite, J. R., Isaacman-VanWertz, G., Kreisberg, N. M., Knote, C., Olson, K., Koss, A., Goldstein, A. H., Hering, S. V., De Gouw, J., Baumann, K., Lee, S.-H., Nenes, A., Weber, R. J., and Ng, N. L.: Effects of anthropogenic emissions on aerosol formation from isoprene and monoterpenes in the southeastern United States, Proceedings of the National Academy of Sciences, 112, 37–42, 2015.

Yan, C., Nie, W., Äijälä, M., Rissanen, M. P., Canagaratna, M. R., Massoli, P., Junninen, H., Jokinen, T., Sarnela, N., Häme, S. A. K., Schobesberger, S., Canonaco, F., Yao, L., Prévôt, A. S. H., Petäjä, T., Kulmala, M., Sipilä, M., Worsnop, D. R., and Ehn, M.: Source characterization of highly oxidized multifunctional compounds in a boreal forest environment using positive matrix factorization, Atmospheric Chemistry and Physics, 16, 12 715–12 731, 2016.

Yu, F. and Luo, G.: Simulation of particle size distribution with a global aerosol model: contribution of nucleation to aerosol and CCN number concentrations, Atmospheric Chemistry and Physics, 9, 7691–7710, 2009.

Zhang, X., Cappa, C. D., Jathar, S. H., McVay, R. C., Ensberg, J. J., Kleeman, M. J., and Seinfeld, J. H.: Influence of vapor wall loss in laboratory chambers on yields of secondary organic aerosol, Proceedings of the National Academy of Sciences, 111, 5802–5807, 2014.

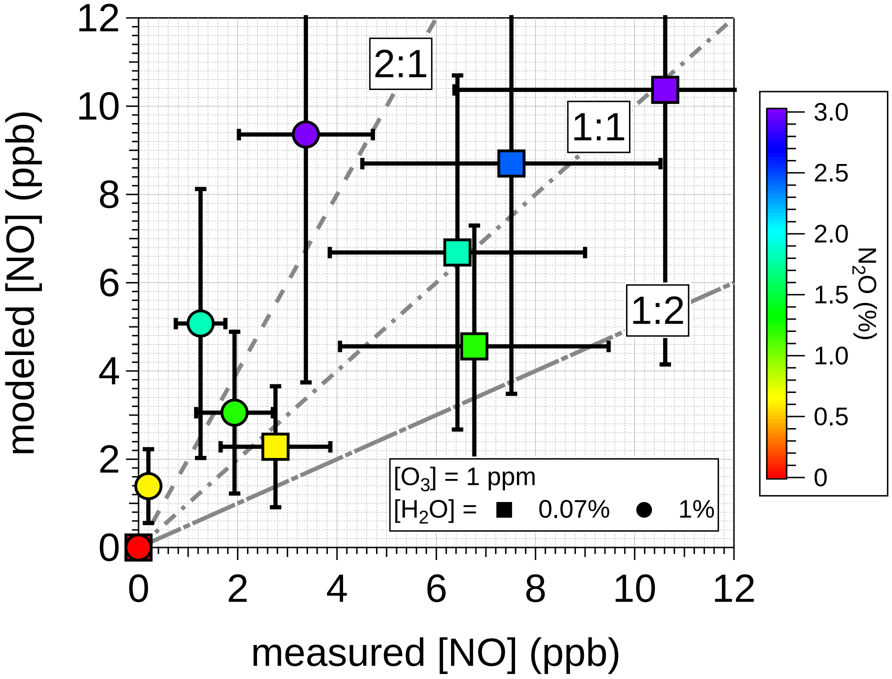

Figure 1. Scatter plot comparing measured and modeled [NO] at 80 sec residence time in the PAM oxidation flow reactor, $I_{254} = 4\times10^{15}$ ph cm^{-2} sec^{-1}, $[O_3]$ = 1 ppm, $[H_2O]$ = 0.07 and 1%, $[N_2O]$ = 0 to 3%. Symbols are colored by $[N_2O]$, with 1:2, 1:1 and 2:1 lines shown for reference. Error bars represent ±60% uncertainty in model outputs (Peng et al., 2015) and ±40% precision in replicate [NO] measurements at fixed $[N_2O]$.

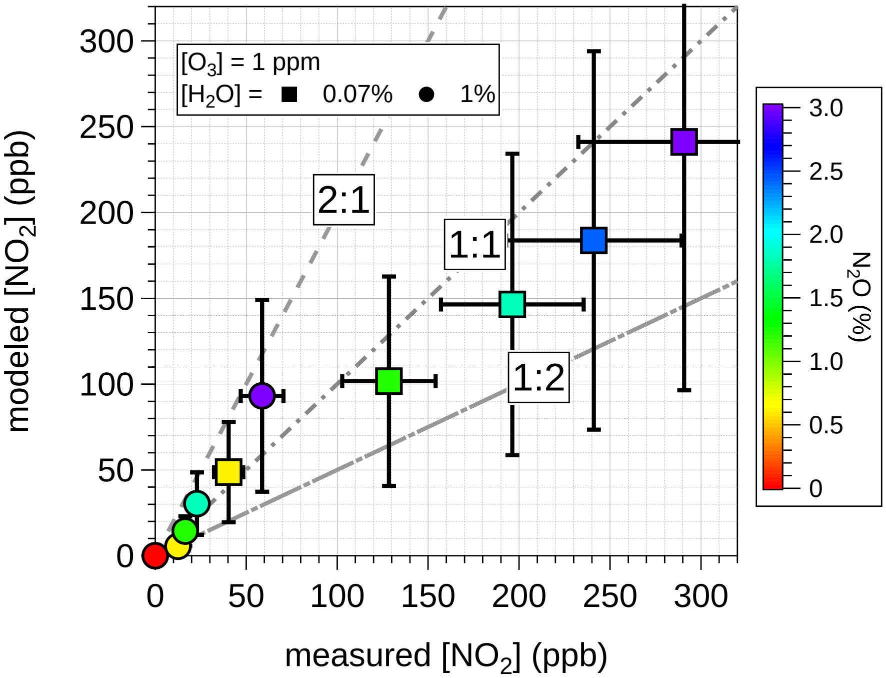

Figure 2. Scatter plot comparing measured and modeled $[NO_2]$ at 80 sec residence time in the PAM reactor, $I_{254} = 4\times10^{15}$ ph cm^{-2} sec^{-1}, $[O_3]$ = 1 ppm, $[H_2O]$ = 0.07 and 1%, $[N_2O]$ = 0 to 3%. Symbols are colored by $[N_2O]$, with 1:2, 1:1 and 2:1 lines shown for reference. Error bars represent ±60% uncertainty in model outputs (Peng et al., 2015) and ±20% precision in replicate [NO] measurements at fixed $[N_2O]$.

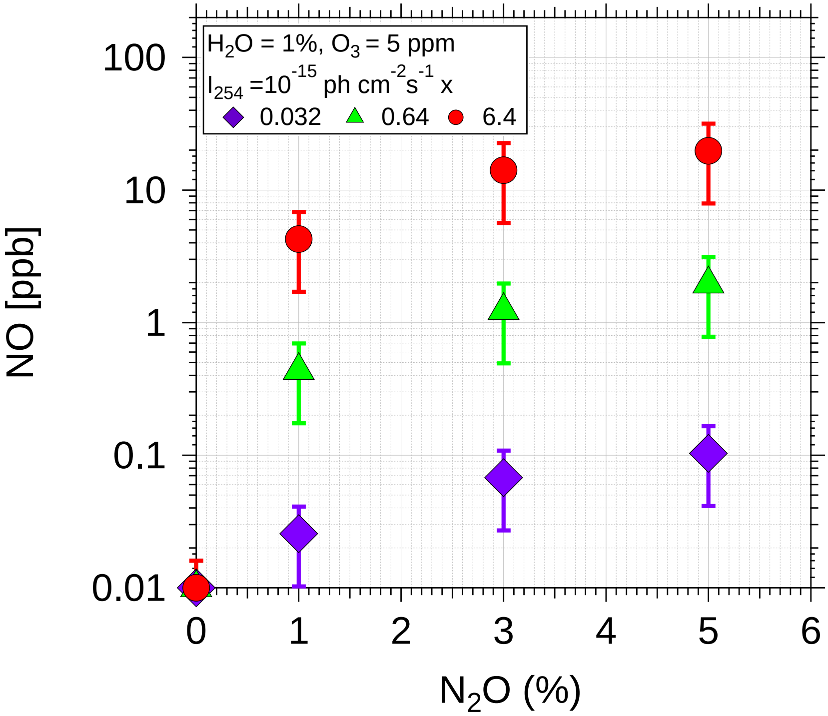

Figure 3. Modeled steady-state [NO] as a function of [N_2O] input to the PAM reactor at I_{254} = 0.032×10^{15}, 0.64×10^{15} and 6.4×10^{15} ph cm^{-2} sec, [H_2O] = 1%, [O_3] = 5 ppm, mean residence time = 80 sec. Error bars represent ± 60% uncertainty in modeled [NO] (Peng et al., 2015).

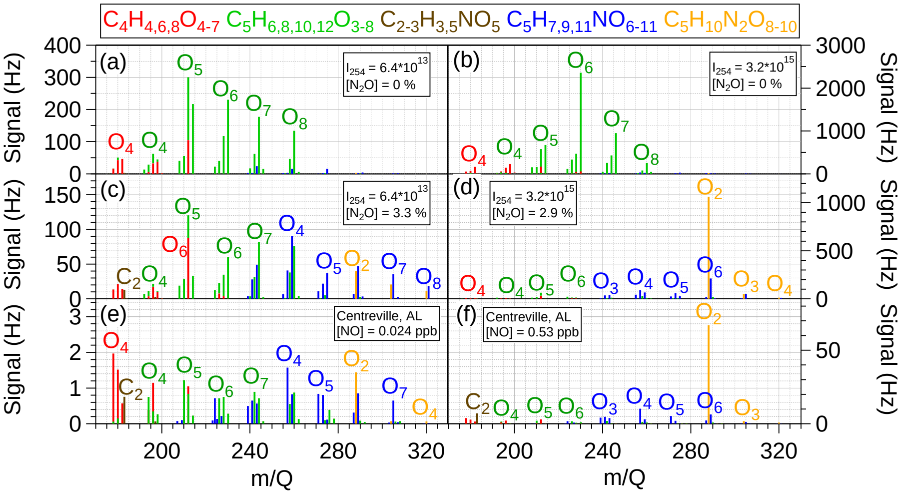

Figure 4. NO_3^--CIMS mass spectra of isoprene oxidation products generated in the PAM reactor at $[H_2O]$ = 1%, $[O_3]$ = 5 ppm, mean residence time = 80 sec: (a) I_{254} = 6.4×10^{13} ph cm^{-2} sec^{-1}, $[N_2O]$ = 0%; (b) I_{254} = 3.2×10^{15} ph cm^{-2} sec^{-1}, $[N_2O]$ = 0 %; (c) I_{254} = 6.4×10^{13} ph cm^{-2} sec^{-1}, $[N_2O]$ = 3.2 %; (d) I_{254} = 3.2×10^{15} ph cm^{-2} sec^{-1}, $[N_2O]$ = 2.9 %. NO_3^--CIMS mass spectra of the same compounds detected at the SOAS ground site in Centreville, Alabama, USA during (e) "low-NO" and (f) "high-NO" conditions (see text for additional details; $C_5H_6O_{5-7}$ ions removed from SOAS spectra due to larger contributions from α-pinene + OH oxidation products (Fig. 6). "C_x" or "O_x" indicates number of carbon or atoms in labeled ions (not including oxygen atoms in nitrate functional groups).

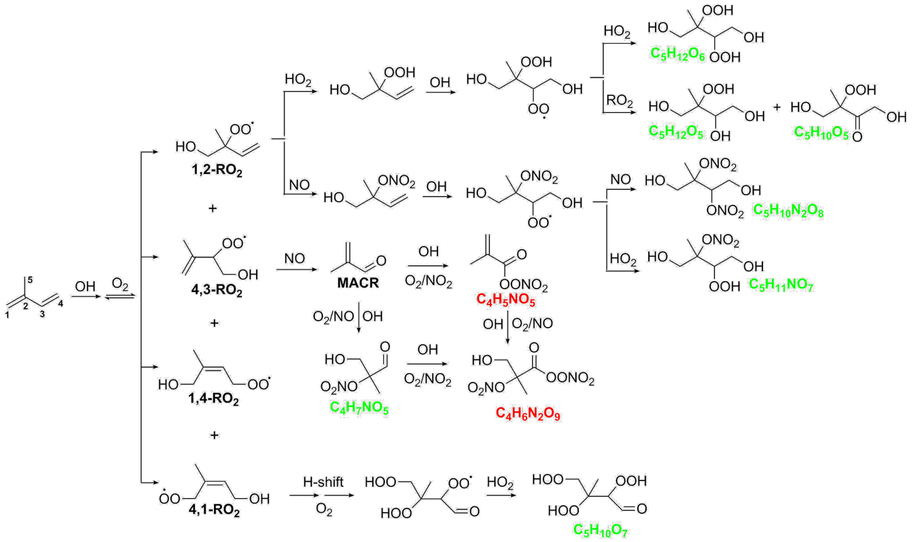

Figure 5. Simplified reaction scheme summarizing known isoprene + OH reaction pathways yielding multigeneration oxidation products. Four peroxy radical ($\mathrm{RO_2}$) isomers are generated following initial OH addition to isoprene: 1,2-$\mathrm{RO_2}$, 4,3-$\mathrm{RO_2}$, 1,4-$\mathrm{RO_2}$, 4,1-$\mathrm{RO_2}$. The 1,2-$\mathrm{RO_2}$ and 4,3-$\mathrm{RO_2}$ isomers follow the same reaction pathways, yielding chemical formulas with green text that were detected with $\mathrm{NO_3^-}$-CIMS. The 4,1-$\mathrm{RO_2}$ isomer yields $\mathrm{C_5H_{10}O_7}$, also detected with $\mathrm{NO_3^-}$-CIMS. Chemical formulas with red text may be generated through the methacrolein (MACR) channel but were not detected with $\mathrm{NO_3^-}$-CIMS .

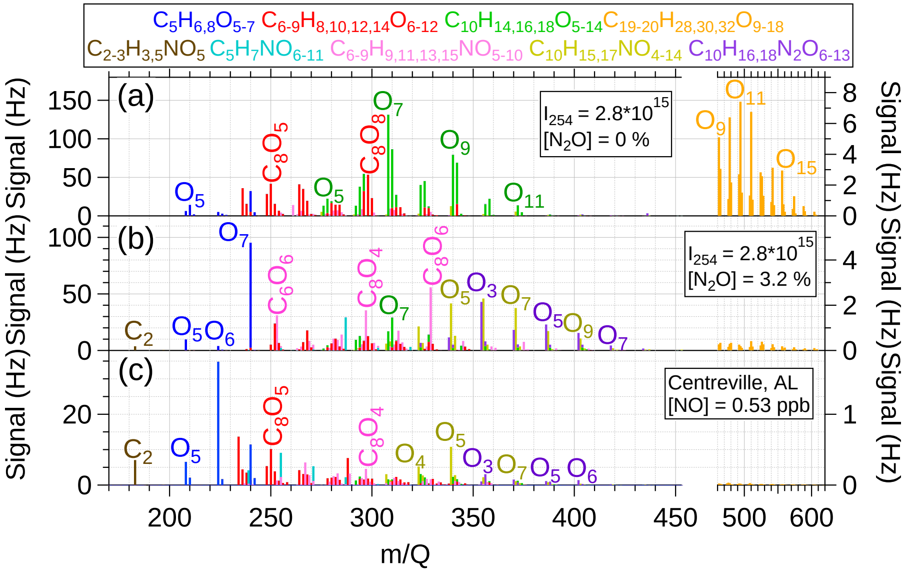

Figure 6. NO_3^--CIMS mass spectra of α-pinene oxidation products generated in the PAM reactor at $[H_2O]$ = 0.07%, $[O_3]$ = 5 ppm, mean residence time = 80 sec: (a) $I_{254} = 2.8\times10^{15}$ ph $cm^{-2}sec^{-1}$, $[N_2O]$ = 0 %; (b) $I_{254} = 2.8\times10^{15}$ ph $cm^{-2}sec^{-1}$, $[N_2O]$ = 3.2 %. (c) NO_3^--CIMS mass spectra of the same compounds detected at the SOAS ground site in Centreville, Alabama, USA during "high-NO" conditions shown in Fig. 4f (note: $C_5H_7NO_{6-11}$ signals in SOAS spectra also contributed from isoprene + OH oxidation products). "C_x" or "O_x" labels indicate number of oxygen atoms in corresponding signals (not including oxygen atoms in nitrate functional groups).

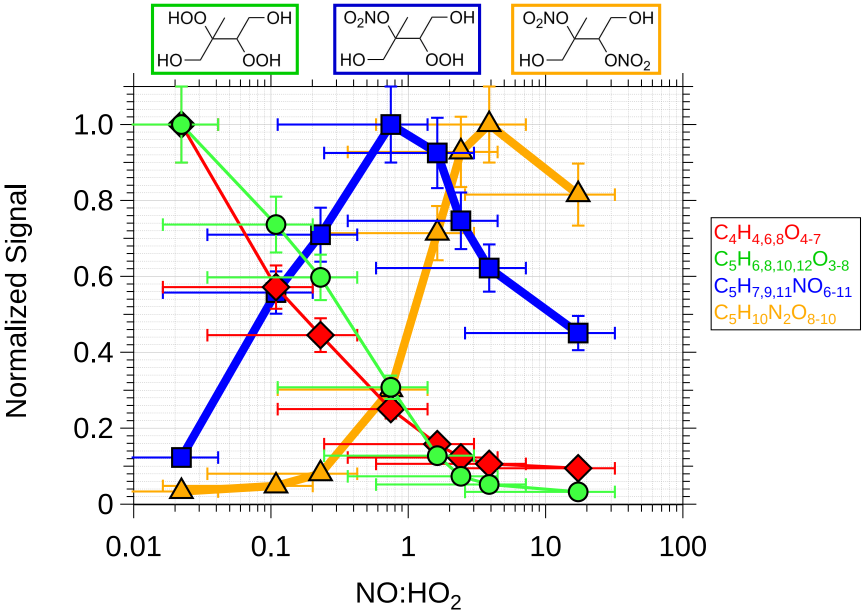

Figure 7. Normalized NO_3^--CIMS signals of $C_4H_{4,6,8}O_{4-7}$, $C_5H_{6,8,10,12}O_{3-8}$, $C_5H_{7,9,11}NO_{6-11}$, and $C_5H_{10}N_2O_{8-10}$ isoprene oxidation products generated in the PAM reactor at I_{254} = 3.2×10^{15} ph cm^{-2} sec^{-1}, $[H_2O]$ = 1%, $[O_3]$ = 5 ppm, mean residence time = 80 sec as a function of modeled $NO:HO_2$. For each of the species classes, signals were normalized to the maximum signal. Proposed structures for $C_5H_{12}O_6$, $C_5H_{11}NO_7$, and $C_5H_{10}N_2O_8$ signals are shown as representative compounds for each species class (Fig. 5). Representative error bars indicate ± 1σ uncertainty in NO_3^--CIMS signals and ± 85% uncertainty in $NO:HO_2$.

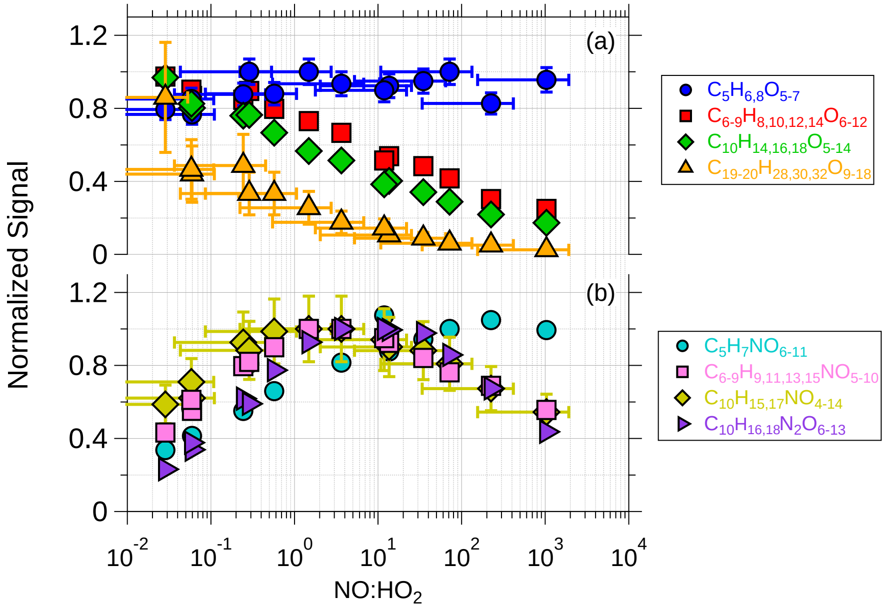

Figure 8. Normalized NO_3^--CIMS signals of (a) $C_5H_{6,8}O_{5-7}$, $C_{6-9}H_{8,10,12,14}O_{6-12}$, $C_{10}H_{14,16,18}O_{5-14}$, $C_{19-20}H_{28,30,32}O_{9-18}$ and (b) $C_5H_7NO_{6-11}$, $C_{6-9}H_{9,11,13,15}NO_{5-10}$, $C_{10}H_{15,17}NO_{4-14}$, and $C_{10}H_{16,18}N_2O_{6-13}$ α-pinene oxidation products generated in the PAM reactor at I_{254} = 2.8×10^{15} ph cm^{-2} sec^{-1}, $[H_2O]$ = 0.07%, $[O_3]$ = 5 ppm, mean residence time = 80 sec as a function of modeled NO:HO_2. For each of the species classes, signals were normalized to the maximum signal. Representative error bars indicate $\pm$ 1σ uncertainty in NO_3^--CIMS signals and ± 85% uncertainty in modeled NO:HO_2.